

Perspectives on lung visualization: Three-dimensional anatomical modeling of computed and micro-computed tomographic data in comparative evolutionary morphology and medicine with applications for COVID-19

Emma R. Schachner¹  | Adam B. Lawson²  | Aracely Martinez³  |
Clinton A. Grand Pre³  | Carl Sabottke⁴  | Farid Abou-Issa³  | Scott Echols⁵  |
Raul E. Diaz Jr⁶  | Andrew J. Moore⁷  | John-Paul Grenier⁸  |
Brandon P. Hedrick⁹  | Bradley Spieler¹⁰ 

¹Department of Physiological Sciences, College of Veterinary Medicine, University of Florida, Gainesville, Florida, USA

²Department of Structural and Cellular Biology, School of Medicine, Tulane University, New Orleans, Louisiana, USA

³Department of Cell Biology and Anatomy, School of Medicine, Louisiana State University Health Sciences Center, New Orleans, Louisiana, USA

⁴Department of Medical Imaging, University of Arizona College of Medicine, Tucson, Arizona, USA

⁵The Medical Center for birds, Oakley, California, USA

⁶Department of Biological Sciences, California State University Los Angeles, Los Angeles, California, USA

⁷Department of Anatomical Sciences, Renaissance School of Medicine, Stony Brook University, New York, New York, USA

⁸Department of Diagnostic, Molecular and Interventional Radiology, Icahn School of Medicine at Mount Sinai, New York, New York, USA

⁹Department of Biomedical Sciences, College of Veterinary Medicine, Cornell University, Ithaca, New York, USA

¹⁰Department of Radiology, University Medical Center, Louisiana State University Health Sciences Center, New Orleans, Louisiana, USA

Correspondence

Emma R. Schachner, Department of Physiological Sciences, College of Veterinary Medicine, University of Florida, Gainesville, FL 32603, USA.
Email: eschachner@ufl.edu

Funding information

Louisiana State University Health Sciences Center Research Enhancement Program Grant

Abstract

The vertebrate respiratory system is challenging to study. The complex relationship between the lungs and adjacent tissues, the vast structural diversity of the respiratory system both within individuals and between taxa, its mobility (or immobility) and distensibility, and the difficulty of quantifying and visualizing functionally important internal negative spaces have all impeded descriptive, functional, and comparative research. As a result, there is a relative paucity of three-dimensional anatomical information on this organ system in all vertebrate groups (including humans) relative to other regions of the body. We present some of the challenges associated with evaluating and visualizing the vertebrate respiratory system using computed and micro-computed tomography and its subsequent digital segmentation. We discuss common mistakes to avoid when imaging deceased and live specimens and various methods for merging manual and threshold-based segmentation approaches to visualize pulmonary tissues across a broad range of vertebrate taxa, with a particular focus on sauropsids (reptiles and birds). We also address some of the recent work in comparative evolutionary morphology and medicine that have used

these techniques to visualize respiratory tissues. Finally, we provide a clinical study on COVID-19 in humans in which we apply modeling methods to visualize and quantify pulmonary infection in the lungs of human patients.

KEYWORDS

anatomy, bird, bronchial tree, computed tomography, pulmonary, respiratory, segmentation

1 | INTRODUCTION

There has been a revolution in comparative anatomy through the three-dimensional (3D) visualization and analysis of tissues over the past 20 years as micro-computed tomography (μ CT), magnetic resonance imaging (MRI), 3D serial section, and computer segmentation have become accessible to a wide variety of researchers. This has particularly been true for work on the head, especially skulls, and cardiovascular systems of vertebrates (Gignac & Kley, 2018; Holliday et al., 2013; Holliday et al., 2022; Metscher, 2009a; Witmer et al., 2008). Although it is relatively simple to visualize hard tissues like bone, reconstructing soft tissues (e.g., nerve, muscle) is difficult due to their low x-ray attenuation. Metscher (2009a, 2009b) developed a method for increasing soft-tissue contrast in CT scans using a solution of iodine (I_2KI), which has since evolved into an inexpensive technique termed diffusible iodine-based contrast-enhanced CT (diceCT) (Gignac et al., 2016). As a result, there has been a recent push to generate 3D soft-tissue models of a variety of organisms ranging from invertebrates (e.g., Metscher, 2009a) to reptiles (e.g., George & Holliday, 2013), birds (e.g., Tahara & Larsson, 2013), mammals (e.g., Aslanidi et al., 2012; Hall et al., 2021; Hedrick et al., 2018; Herdina et al., 2010), among others. Despite the explosion in studies of both hard and soft tissues, the creation of 3D models of pulmonary tissues has received considerably less attention, particularly in nonhuman species. Indeed, with the exception of domesticated mammals commonly treated by the veterinary community or utilized in medical research, for example, murine, ovine, porcine, and primate models (Bauer et al., 2012; Carson et al., 2010; Glennly et al., 2020; Tawhai et al., 2004) and select cetaceans (Ivancic et al., 2014; Moore et al., 2011), very few high fidelity 3D pulmonary models exist for nonhuman vertebrates.

The dearth of high-resolution 3D comparative anatomical data on vertebrate pulmonary systems is the result of several factors. These include difficulties in visualizing negative spaces (rather than hard or soft tissues such as bone and muscle), the delicate nature of respiratory tissues, the speed at which lungs decay in postmortem specimens, the need for lungs to be inflated and to maintain inflation throughout imaging, and the vast

structural diversity of the vertebrate respiratory system (Figure 1). Additionally, because the lung is a mobile distensible organ that moves during ventilation, scans only represent one snapshot of its morphological conformation during the ventilatory cycle. As a result, the timing of the scan during the ventilatory cycle can dramatically impact the size and shape of some pulmonary tissues in live scans, whether due to normal breathing or due to the scan being taken during an apnea (breath hold). In deceased subjects, relative inflation of the pulmonary tissues can be controlled by the researcher, but this presents its own set of challenges and considerations (see below). Moreover, the relationship between the respiratory system and adjacent organs, like the gastrointestinal system, or between the lungs and the skeletal system, can also have a dramatic impact on the morphology of the pulmonary tissues, particularly in birds. All of these features have made the respiratory system particularly challenging to study, image, and model in three dimensions.

In this review, we evaluate some of the known challenges associated with visualizing the vertebrate respiratory system in 3D using CT, μ CT, and digital segmentation, both in the context of evolutionary and comparative biology as well as human and veterinary medicine. We illustrate some of the proposed solutions to demonstrate how threshold-based segmentation and manual segmentation can be merged to visualize a pulmonary infection, providing an intuitive method for communicating the impact of disease to the public and quantifying the infectious load in the lungs.

2 | THE IMPACT OF SPECIMEN STATE AND PREPARATION

In live scans, normal ventilation during imaging can present a major complication. Depending upon the taxon imaged, whether or not they are anesthetized, which anesthetic is used, body position during the scan, and the health of the individual, the impact on the lungs will vary (Garcia-Sanz et al., 2020; Asorey et al., 2020; Escobar et al., 2016; Malka et al., 2009; Williams et al., 2021). As the mammalian bronchoalveolar lung is tidally ventilated and flexible (Meyer et al., 1981), the problem is more

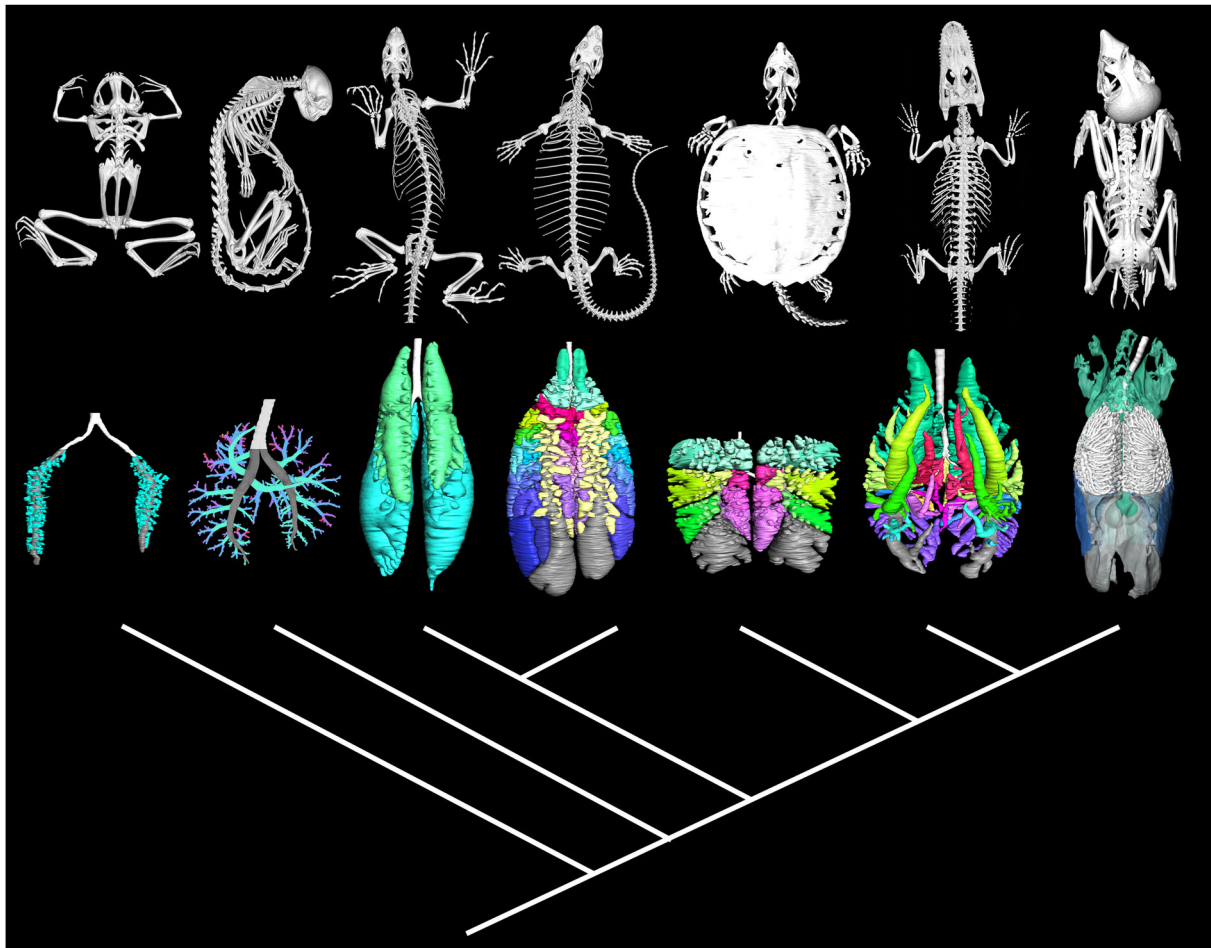


FIGURE 1 Cladogram for tetrapods with segmented models demonstrating the structural diversity of the respiratory system (modified from Schachner et al., 2021). From left to right: African clawed frog (*Xenopus* sp.), a tamarin (*Saguinus* sp.), a green iguana (*Iguana iguana*), a savannah monitor lizard (*Varanus exanthematicus*), a snapping turtle (*Chelydra serpentina*), an American alligator (*Alligator mississippiensis*), and a zebra finch (*Taeniopygia guttata*).

spatially diffuse than in the heterogeneously ventilated lungs of diapsids, but in both cases, warping of pulmonary tissue during ventilation results in the blurring of tissue boundaries. In birds, the gas-exchanging portion of the lung is immobilized and dorsally positioned within the thoracic cage and ventilation occurs due to the depression of the sternum (Powell, 2015). Due to this more localized movement, normal ventilation during the scan predominantly disrupts imaging of the cervical and interclavicular air sacs. In both birds and reptiles, movement of the cardiac tissues can impact pulmonary tissues adjacent to the heart and great vessels. Cardiac movement particularly impacts pulmonary imaging in the region of the cardiac lobes in crocodylians, saccular regions of the lung in squamates, and air sacs surrounding the heart in birds. Studies of live sedated birds have demonstrated that body positioning can also impact pulmonary imaging, such that birds scanned in dorsal recumbency (i.e., the supine position) show diminished

lung and air sac volumes due to the impact of the viscera on the caudal sacs (Malka et al., 2009; Nevitt et al., 2014). Dorsal recumbency produces similar shape changes in the lung of *Alligator mississippiensis* (Schachner et al., 2021) and reduces lung volume in *Trachemys scripta scripta* (Williams et al., 2021), but it is not known whether body position impacts pulmonary imaging in other non-archosaurian diapsids.

For comparative anatomy projects, specimens are commonly collected via salvage (i.e., found naturally deceased), and thus the time between death and preservation or freezing is often unknown. Though this is not a problem for evaluating skeletal morphology, pulmonary tissues quickly degrade such that there is a small window of time in which they are usable. For avian specimens in particular, the thin air sacs degrade (Figure 2b) and the bronchial tree and parenchyma fill with fluid (Figure 2b), making respiratory data unusable in a specimen that might still be acceptable for a musculoskeletal project

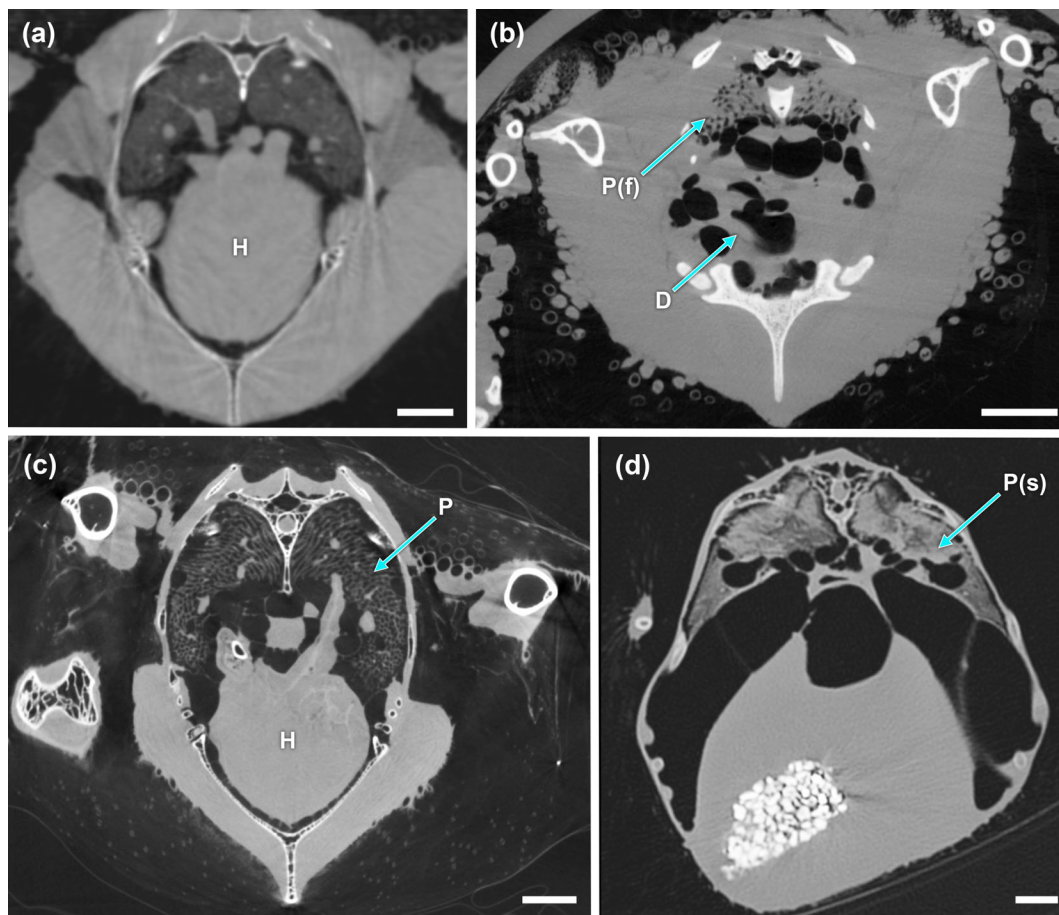


FIGURE 2 Axial sections of computed tomography (CT) images of birds demonstrating a range of possible pulmonary observations. (a) A live sedated peregrine falcon (*Falco peregrinus*) scanned at 250 μm ; (b) a deceased juvenile red-shouldered hawk (*Buteo lineatus*) with decaying pulmonary tissues, rotting cervical and interclavicular air sacs, and fluid in the parabronchi scanned at 82 μm ; (c) a deceased subadult red-tailed hawk (*Buteo jamaicensis*) with extremely well preserved lungs and clear parabronchi scanned at 133 μm ; (d) a deceased juvenile ostrich (*Struthio camelus*; from Schachner et al., 2021) with lungs that have been diceCT stained and have fluid trapped in the parabronchi scanned on a medical grade CT scanner at 600 μm . D, decay; H, heart; P, parabronchi; P(f), parabronchi with fluid; P(s), parabronchi stained via diceCT. The lungs of the deceased birds have been inflated until a natural resistance was felt. Scale bar = 1 cm.

and seemingly fine when inspected after collection. To our knowledge, there are no known studies documenting the rate of decay for pulmonary tissues in different phylogenetic groups; however, research has shown substantial changes occur in the pulmonary cell boundary after 8 h at 25°C in murine models (Pattle et al., 1974), and in CT scanned avian specimens, we have observed substantial gross decay within a comparable timeframe. Another important consideration is potential respiratory disease or pathology. For human clinical scans, this information will have been reported in the patient data. However, with nonhuman vertebrate specimens, disease status is not always reported. In a deceased specimen, lung decay and pulmonary infection will look very similar in a scan. Sauropsids are susceptible to respiratory disease ranging from viruses to pulmonary tumors, particularly in captivity (Driggers, 2000; Gumpenberger, 2021; Hoon-Hanks

et al., 2020; Schumacher, 2003), and thus fluid in the lungs may have resulted from disease and not be apparent until after imaging.

For live scans, the imaging data capture the lung somewhere within its inspiratory capacity (i.e., normal tidal volume + inspiratory reserve volume). Ideally, imaging takes place during an apnea, to minimize blurring of tissue boundaries due to movement. Time related changes in the appearance of pulmonary tissue secondary to respiratory motion can be captured with four-dimensional (4D) CT, which is essentially CT with the added component of temporal data. 4D CT imaging (in medicine) can be acquired prospectively or, retrospectively, employing gated/breath hold as well as free breathing techniques (Hugo & Rosu, 2012). With deceased specimens, unless the aim is to evaluate the structure of the lungs in a state of reduced inflation,

intubation and inflation is required prior to scanning and the lungs are inflated close to (or at) maximum inspiratory capacity (for some examples, see e.g., Lawson et al., 2021; Schachner et al., 2013; Schachner et al., 2014; Schachner et al., 2021). To achieve a tight seal, it is often necessary to perform a tracheostomy bypassing the glottis, particularly in small specimens like hummingbirds or chameleons who have a complex hyoid apparatus. Polyethylene tubing is inserted directly into the trachea and sutured or glued in place, and a stopcock and an appropriately sized syringe are attached to the tubing (Figure 3). The animal is then manually inflated with the syringe until the researcher feels gentle resistance (or measures the appropriate pressures). The air tightness of the seal can be tested by submerging the specimen in water and checking for bubbles. Care must be taken not to overinflate the specimen, as this risks abnormal distension or rupturing of the pulmonary tissues. In birds, ruptured respiratory tissues can be identified in the imaging data by looking for large asymmetric expansions of the pulmonary diverticula that extend beyond the normal respiratory boundaries in between and around the muscles and under the skin, coupled with torn or frayed tissues.

Although diceCT is very effective for visualizing soft tissues (e.g., brain, muscles), very little work has been done to evaluate the impact of diceCT on pulmonary tissues. However, it is noteworthy that most tissues stained using diceCT methodology are fixed in phosphate-buffered formalin solutions prior to staining (Gignac et al., 2016), which increases tissue stiffness and reduces the ability to inflate the lungs for scanning. Another common method for contrast staining embryonic and adult tissues is 3–4% phosphotungstic acid (see, e.g., Molnar et al., 2017); however, to our knowledge, this method has not yet been used to visualize lungs in juvenile or adult vertebrates.

3 | TYPES OF IMAGING DATA AND IMAGING SOFTWARE

In the paleontological and morphological sciences, both Tag Image File Format (TIFF) and Digital Imaging and Communications in Medicine (DICOM) files are used for quantitative and qualitative analyses. However, DICOM files and other 3D data formats such as the Neuroimaging Informatics Technology Initiative (NIfTI) file format have

FIGURE 3 Preparation of a specimen for micro-computed tomography (μ CT) scanning. (a) Intubation of a hatchling duck with a small diameter polyethylene tube directly into the trachea, bypassing the glottis. (b) Intubation of an adult hummingbird (*Calypte anna*) into the trachea using a catheter that has been attached to a stopcock so that the lungs can be inflated and sealed. (c) An iPhone photo of the screen showing the projection of the *C. anna* just prior to scanning with the lungs inflated. (d) Intubated and inflated hawk that has been prepared for scanning in a Nikon XT H 225ST. Images were prepared in Adobe Photoshop (Adobe Inc.).

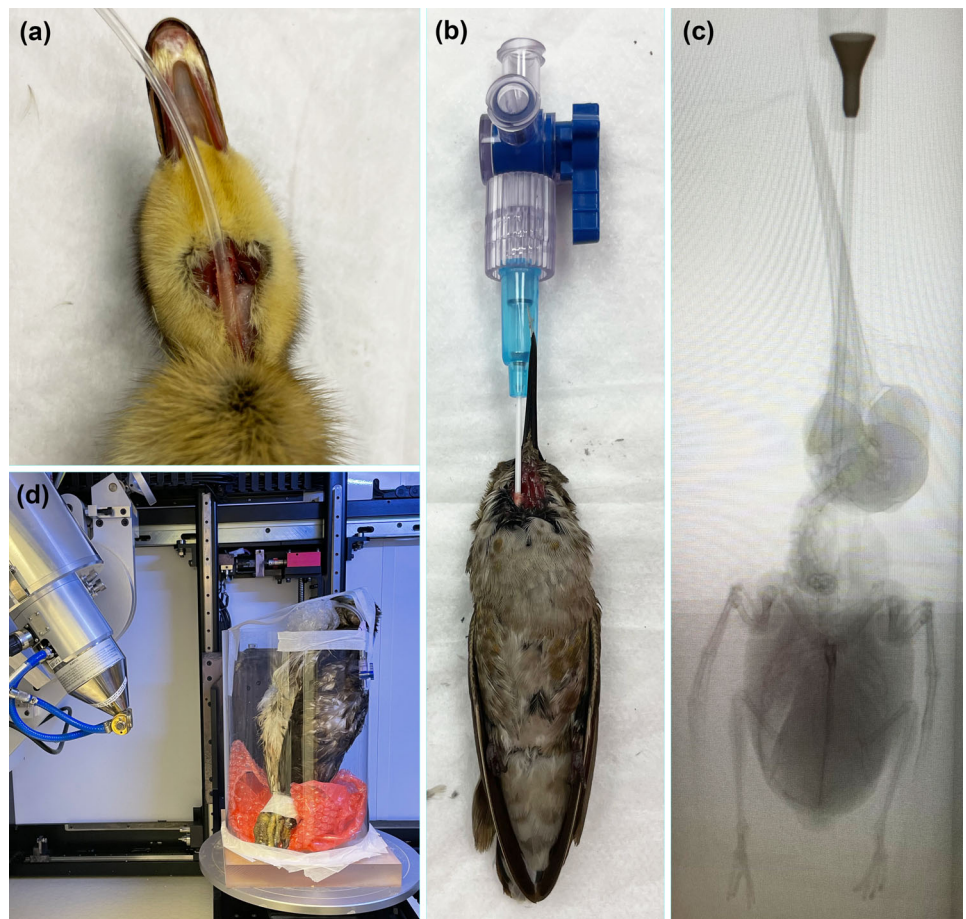


TABLE 1 Commonly used software programs for segmenting and visualizing pulmonary data.

Software	Publisher	Cost estimate	Open source (Y/N)	Operating system	Notes
Avizo/Amira	Thermo Fisher Scientific	>\$7k/license with annual maintenance fee	No	Windows, Linux	
VGSTUDIO	Volume Graphics (Hexagon)	>\$13k/license with annual maintenance fee	No	Windows	VGSTUDIO MAX also accommodates Linux and Mac users
Dragonfly	Object Research Systems	Free for noncommercial users	No	Windows, Linux	DICOM or image stack editor; useful for volume rendering
Mimics	Materialize	>\$10k/license with annual maintenance fee	No	Windows	FDA approved module
ITK-SNAP	GNU General Public License	Free	Yes	Windows, Linux, Mac OS	
3D Slicer	The Slicer Community	Free	Yes	Windows, Mac OS, Linux	Not approved for clinical use
OsiriX	Pixmeo	From \$69.99/mo.	Yes	Mac OS	DICOM editor; useful for volume rendering
Horos	Horos Project	Free	Yes	Mac OS	DICOM editor; primarily useful for volume rendering

advantages over the two-dimensional (2D) TIFF image format, the most distinct being that DICOM data maintain connectivity with other software programs and scanners if properly encoded (i.e., the metadata are included). Although NIfTI was originally developed for neuroimaging, it has found broader use for 3D medical image research and, for example, multiple lung segmentation CT datasets for COVID-19 patients (see, e.g., <https://wiki.cancerimagingarchive.net/display/Public/CT+Images+in+COVID-19>) utilize the NIfTI format for data sharing (Harmon et al., 2020; Kassin et al., 2021). A disadvantage of 2D TIFF files compared to DICOM and NIfTI formats is that TIFF files lack embedded metadata about scan resolution (i.e., pixel dimensions and slice thickness), which are required to determine accurate voxel size for 3D applications. Additionally, many segmentation programs lack features that permit TIFF imports (e.g., OsiriX MD; Rosset et al., 2004; <https://www.osirix-viewer.com>). In contrast, other platforms, like Dragonfly (Object Research Systems Inc., Montréal, Canada; <https://www.theobjects.com/dragonfly/index.html>), permit the user to import either DICOM or image stacks. Users may find themselves limited by their preferred operating system; many platforms are available only for certain systems

(e.g., OsiriX MD and Horos only run on Mac, whereas Dragonfly runs on Windows and Linux), although some, like 3D slicer (<https://www.slicer.org/>; Fedorov et al., 2012), are available on all three major operating systems. For a comparison between the most commonly used software programs for segmentation and volume rendering of pulmonary tissues, see Table 1.

Scan resolution and slice thickness together inform the voxel width, length, and height of a given image stack, and so directly impact the level of possible detail that can be analyzed and visualized in 3D. Typically, scan resolution and slice thickness values match in MR and CT image stacks, generating cubic (i.e., isometric) voxels, but may be different in certain types of nonuniform image stacks (e.g., histological slides or merged data from multiple scans of the same specimen). Medical grade scanners are usually capable of a minimum of 0.5–0.7 mm slice thickness, although radiologist interpretation in human patients is often performed with a reconstructed slice thickness of 1–2 mm to improve the signal-to-noise ratio of the region of interest under review (Bhalla et al., 2019). However, due to fewer constraints related to radiation dose, some specialty in vivo live animal μ CT scanners will export DICOMs that have a slice thickness from approximately 250 μ m to just a few μ m.

4 | TYPES OF VISUALIZATION AND SEGMENTATION, AND ASSOCIATED CHALLENGES

In addition to scan quality/resolution and software functionality, the choice of 3D visualization is made based on what aspect of the image stack needs to be visualized for a particular application (Figure 4) (for a recent review, see Xu et al., 2021). A variety of algorithms work relatively efficiently to represent pixel intensity values directly from the 2D stack as a 3D volume. Algorithms that render all intensity values, in most medical imaging, will generate visualizations of both soft and hard tissues (Drebin et al., 1988) that, consequently, will partially obscure one another. Volume rendering preserves volumetric intensity data that are obscured, and in many applications, can be revealed by interactively “slicing” the 3D visualization. Volume rendering requires little time investment to implement, and has been used to effectively visualize the lungs of numerous taxa (e.g., frogs, iguanas, snakes, tortoises, rabbits), and the thoracoabdominal viscera of humans and other vertebrates, including Egyptian mummies (Cieri et al., 2014; Farmer, 2017, 2021; Hawass & Saleem, 2016) exposing a realistic rendering of the internal structure of the lungs, including in specimens that were contrast injected prior to scanning (Figure 5h,i). 3D maximum intensity projections (MIPs) can isolate tissue types by visualizing internal structures comprised only of voxels with the greatest intensities (e.g., bone or metal in CT). The quality of these visualizations is dependent on the

contrast between the desired object and other regions of the image stack data (Wallis & Miller, 1991). For example, similarly intense pixel values for other structures in the scan (e.g., the scanning bed, medical equipment) may obscure metal or bone. Tissues with lower intensities (e.g., air-filled lungs) or poor tissue contrast (e.g., blood and fat in CT) can be visualized with other algorithms, although they more often are restricted in their use to 2D diagnostic evaluations (Booz et al., 2021) or other specialized medical applications (Vergalasova & Cai, 2020).

Segmentation and surface modeling is often implemented at the cost of efficiency and time investment when there is insufficient resolution and/or intensity contrast to isolate, visualize, and illustrate relationships between specific pulmonary tissues or air spaces using volume rendering alone. Image segmentation makes partitions of regions of an image stack for selected 3D visualization (Figure 6), the partitions being chosen based on the desired visualization (e.g., air space, soft tissue structure, or organ surface). Critically, the partitioning need not depend on the intensity values from the image stack and can incorporate user-driven awareness of anatomy into the visualization. As 3D partition shape is not necessarily dependent on intensity values from the image stack, surfaces are often generated to visualize segmented image data. Rather than representing intensity values, 3D partitions are represented as 3D isosurfaces that are then simplified into polygonal mesh surface models, usually comprising minute triangular facets. Importantly, the process of generating polygonal meshes simplifies the

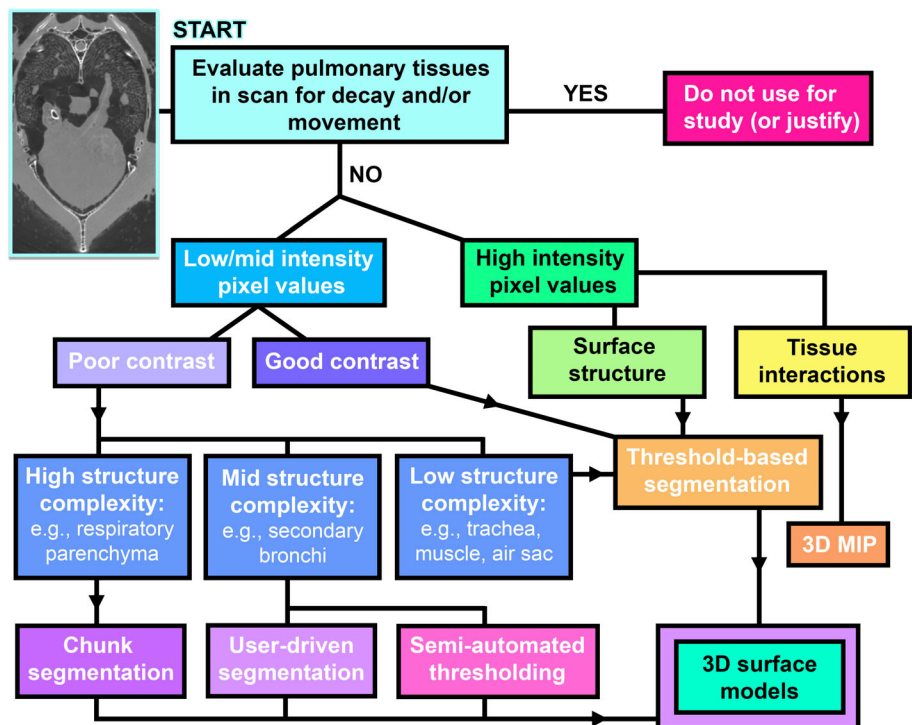


FIGURE 4 Simplified flowchart demonstrating various suggested paths for rendering 3D models from pulmonary imaging data. Note that these are not all of the possible paths, for example, muscles can and often are segmented manually (user-driven segmentation). 3D, three-dimensional; MIP, maximum intensity projection.

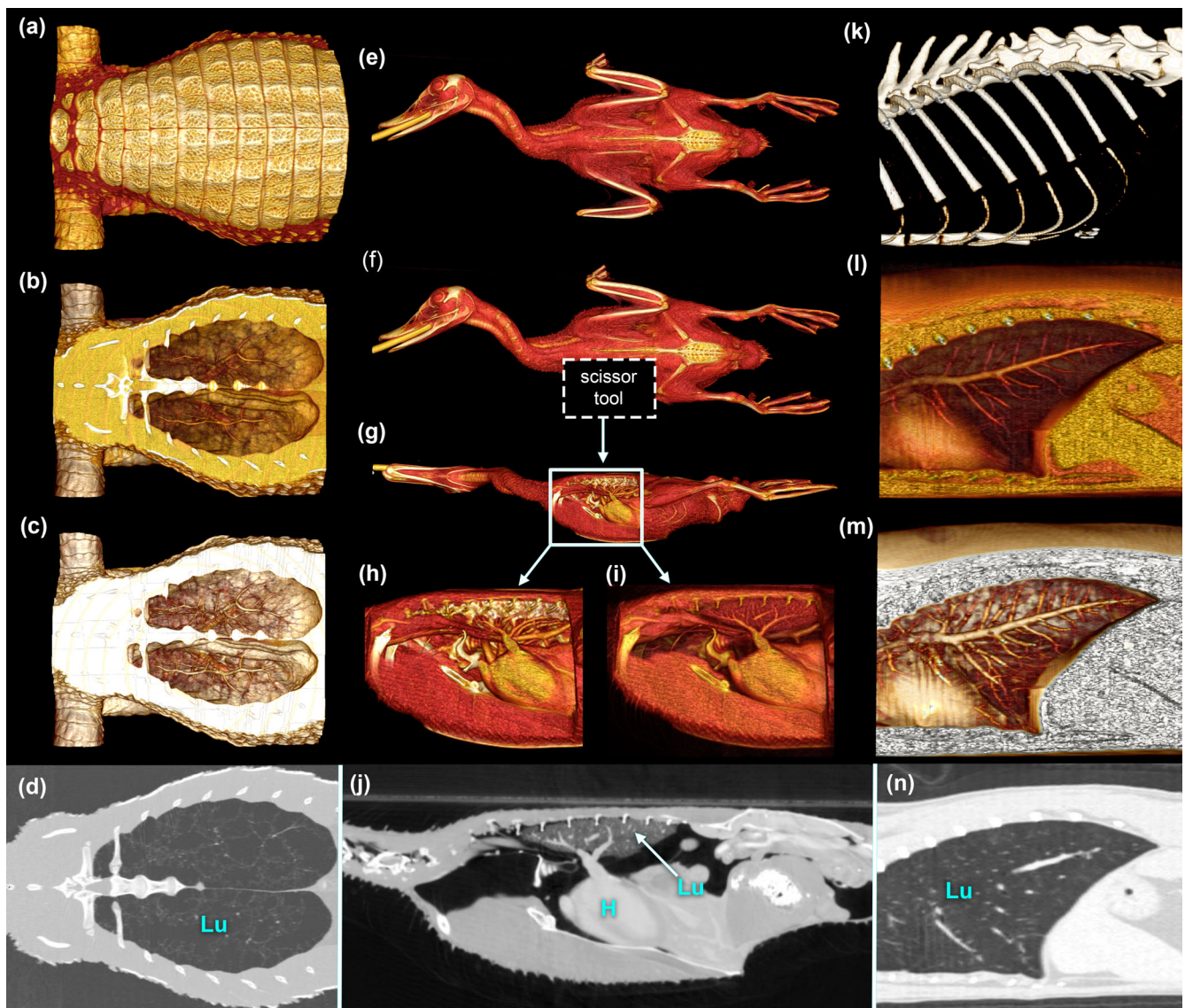


FIGURE 5 Volume rendered models of the respiratory system of three different live amniotes. (a–c) Dorsal view of an adult live sedated Cuvier's dwarf caiman (*Paleosuchus palpebrosus*) scanned at 1.25 mm, with the scutes and vertebrae sliced off so that the vasculature can be seen in coronal view in (b) and (c), with the same coronal view demonstrated as a single computed tomography (CT) slice in (d). Dorsal (e, f), and lateral views (g–i) of a redhead duck (*Aythya americana*) with a window cut into the left side of the thorax with the scissor tool in Osirix MD in (f–i) to demonstrate the cardiopulmonary system, rendered at two different levels. (j) A parasagittal CT slice demonstrating the same view as (g) as a single CT slice. The duck was sedated and imaged for clinical purposes unrelated to this study. Left lateral view of a domestic cat (*Felis catus*) thoracic skeleton (k), and thorax with a parasagittal window cut to visualize the cardiopulmonary system (l, m), and a similarly aligned CT slice (n). The cat was sedated and imaged for clinical purposes unrelated to this study. H, heart; Lu, lung.

partition data as a surface model and discards the volumetric data on which it is based. In contrast to volume rendering, the often time-intensive work of segmenting and subsequent surface model generation provides isolated and unambiguous surface illustrations of the data that are ideal for evaluating their overall shape. Analogous to dissection, segmentation reveals relationships in data selectively by pairing the knowledge and expertise of the investigator(s) with applications that work to keep the illustrations grounded in and continuously informed

by image data. Reflective of this, many of the following techniques described for segmentation rely on judicious application of software tools that correspond to the image data parameters used in algorithmically driven direct volume rendering.

Segmentation software programs include a broad range of tools for automated or semiautomated identification of structures, and these have been described elsewhere in great detail (Starmans et al., 2020; Zanaty & Ghoniemy, 2016). Thresholding is the most typically

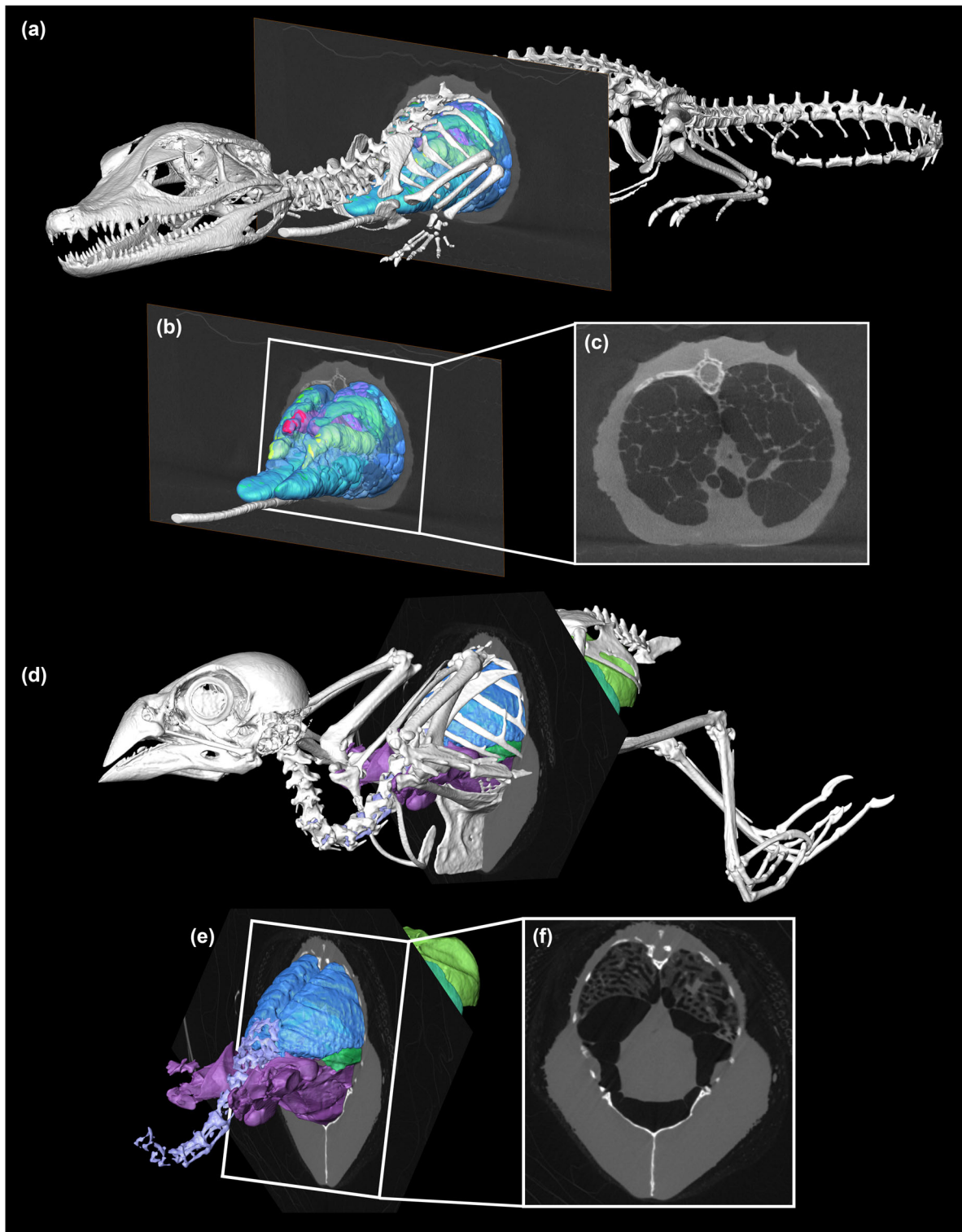


FIGURE 6 Segmented surface models of the skeleton and respiratory systems of a hatchling Cuvier's dwarf caiman (*Paleosuchus palpebrosus*) modified from Schachner et al. (2022) (a–c) and an adult zebra finch (*Taeniopygia guttata*) (d–f) in left craniolateral views demonstrating the relationship between the models and the DICOM image stack.

applied modality for standard segmentation algorithms, in which minimum/maximum threshold pixel intensities are selectively visualized (e.g., as in MIPs). Combined with region-growing/seeding algorithms, pixels can be

selected iteratively for a specific range of intensities only if they are neighbors of previously selected pixels. While these methods can permit isolated segmentation of, for example, a specific bone, they are limited by imaging

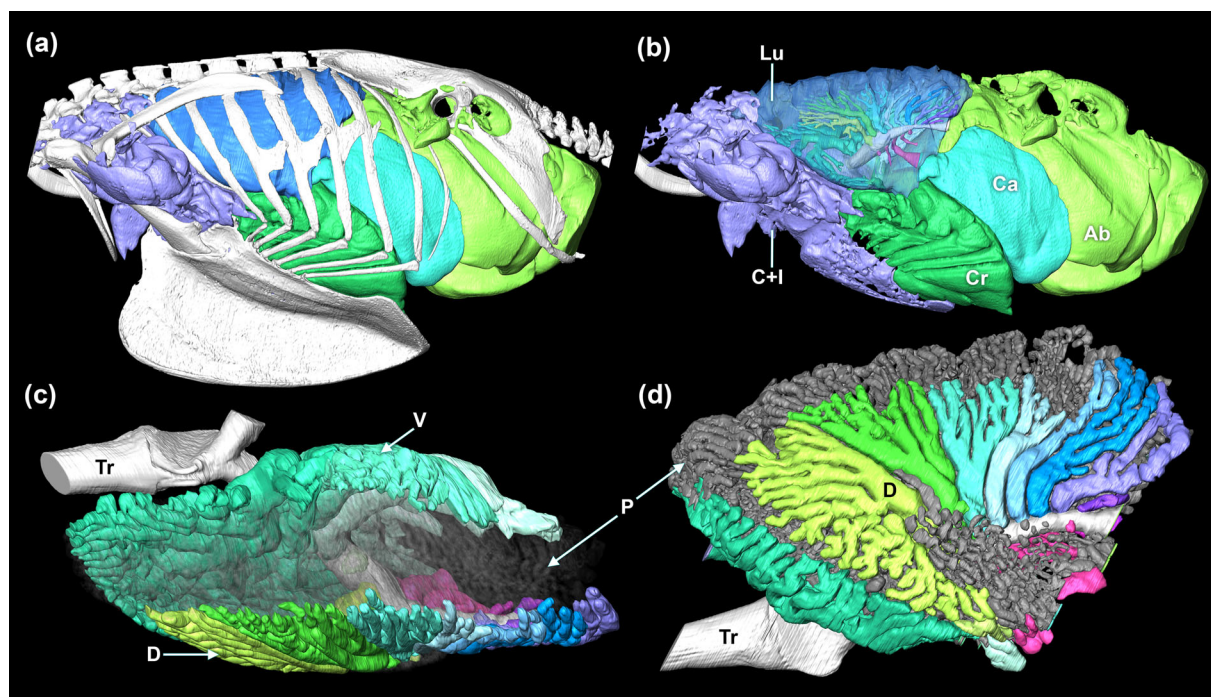


FIGURE 7 Surface model of the thorax and respiratory system of an African gray parrot (*Psittacus erithacus*) segmented from micro-computed tomography (μ CT) data, modified from Lawson et al. (2021). Entire lower respiratory system of *P. erithacus* (artificially inflated postmortem) in left lateral view with (a) and without (b) the thoracic skeleton present, and the gas-exchanging lung surface made semitranslucent in (b) showing a solid model of the large secondary air-conducting tubes, that is, the bronchial tree. A segmented model of the left gas-exchanging lung of a separate specimen of *P. erithacus* generated from a high-resolution μ CT scan (41.08 μ m) in dorsal (c) and left lateral (d) views demonstrating the complete bronchial tree, including the parabronchial network. Ab, abdominal air sac; C, cervical air sac; Ca, caudal thoracic air sac; Cr, cranial thoracic air sac; D, dorsobronchus; I, interclavicular air sac; Lu, gas-exchanging lung surface; Tr, trachea; V, ventrobronchus.

artifacts and resolution. Voxel size, for example, may fail to represent the radiodense boundaries of articulating bones and their more radiolucent synovial joints, resulting in the spread of a region-growing algorithm to whole sections of the adjacent skeleton. To overcome these and other challenges, a variety of more complex algorithms have been employed to more effectively isolate specific tissues (e.g., edge detection, histogram analysis, deep learning applications). These collected algorithms can be applied alone (“automated”) or with limited human intervention (“semiautomated”), but still depend to some degree on tissue contrasts and, in the case of deep learning-based applications, pre-segmented image samples for model training (Hesamian et al., 2019).

In the absence of injected contrasting agents, natural tissue contrasts in the mammalian lung include radiolucent air, radiopaque hyaline cartilage, and the nearly homogenous radiodensities of all the remaining parenchyma. Bronchi are arranged like a tree and ramify into terminal, air-filled sacs. Consequently, the boundaries of the entire lung are a homogenous mixture of soft tissue and air that can be easily isolated from the surrounding soft tissues that lack air (e.g., pleura, ribs, and intercostal

musculature). Internally, visualization of the bronchial and bronchiolar conduits is limited by the resolution of the dataset and its ability to resolve parenchymal septations. Additionally, the lack of contrast between the parenchyma and any fluids present in the lung (e.g., edema, surfactant) limit accurate rendering of the distal aspects of bronchial tree (Figure 2b,d). For example, surface tensions that are sufficient to maintain fluid films in the bronchi and bronchiolar pathways can partition these air conduits into discontinuous regions of radiolucent voxels and may therefore prevent a region-growing algorithm from spreading to distal portions of the air pathways.

The unique arrangement of the avian lung poses even greater challenges for 3D visualization. Unlike the mammalian lung, the large secondary bronchi form a substantial aspect of the superficial surface of the lung in many taxa. Instead of a ramifying tree, the conduits of the avian lung are arranged more like the parallel circuits of a blood-capillary network (Maina, 2017; Maina & Woodward, 2009; Woodward & Maina, 2005, 2008; Woodward et al., 2021). The primary and secondary airways are interconnected by the parabronchi, which

deliver gas to the respiratory parenchyma (made up of a network of air capillaries) (Figure 7c,d). The luminal surfaces of the paleopulmonic parabronchi give rise to atria and infundibula that ultimately give way to the minute air capillaries and their associated blood-capillary network (Maina, 2017). The air sacs originate from sites termed ostia, where the primary bronchus (for the abdominal sacs), secondary bronchi, and parabronchi terminate and occupy spaces in the coelomic cavity. Further, these air sacs invade adjacent bone, occupying the typically marrow-filled regions with air-filled, epithelium-lined, and pneumatic diverticula.

5 | SUGGESTED APPROACH FOR SEGMENTATION OF THE AVIAN RESPIRATORY SYSTEM

In general, advanced segmentation techniques of the avian respiratory system are preceded by a “bulk segmentation” that involves simple region-growing threshold ranges applied to the entire air sac and lung system in the original scan plane. While the scan plane usually approximates axial sections, positioning of the specimen on the gantry often generates more oblique original sections. Region growing is typically performed slice by slice, rather than for the entire image stack, to prevent inclusion of the environmental air and the connected upper respiratory system. The presence of bone and metal in many of the scans also introduces beam hardening and beam attenuation artifacts. Consequently, region-growing algorithms occasionally include unwanted soft tissue and adjacent air (e.g., from the external environment or trapped in the gastrointestinal tract). These unwanted inclusions could be omitted by slightly adjusting threshold ranges or, alternatively, could be manually delabeled. Once the air sacs and gas-exchanging lung are grossly thresholded with a single label, they can be separated into individual air sacs and lung by manually identifying and re-labeling the thin tissue boundaries between sacs. Further advanced techniques can then be employed to segment the air sacs, gas-exchanging lung, and pneumatizing components of the lower respiratory system.

Several of the air sacs often have intertwined and ambiguous boundaries that must be meticulously refined through manual segmentation. To ensure accuracy, these ambiguous tissue boundaries are iteratively reassessed in other orthogonal planes (approximating sagittal and horizontal/coronal cross sections) and relabeled accordingly. In some scans, precise boundaries between air sacs are complex enough that they cannot be separated and are left as a single model (e.g., the interclavicular air sac and bilateral cervical air sacs of the African gray parrot

(*Psittacus erithacus*; Figure 7b)). In birds, segmentation of the gas-exchanging lung involves a variety of advanced techniques that depend on the quality of the scan and the desired level of detail. Once the cranial, ventral, and caudal lung boundaries with the air sacs are defined, soft tissues of the parenchymal lung that were not included in the original thresholding are manually segmented and incorporated into a “lung surface” model. Unlike the air sac boundaries, which represent the air-filled “negative space” of the air sacs, the lung surface model represents a heterogeneous collection of air-filled spaces and parenchyma that comprise the gas-exchanging lung, including bronchi, parabronchi, and the sites where these conduits communicate with the air sacs, as well as pulmonary vasculature. Internally, the heterogeneous mixture of air-filled conduits (bronchi, parabronchi) and their associated parenchyma are often too complex and variable across scans for semiautomated segmentation from CT (however, the gas-exchanging tissues can be reconstructed in high-resolution via serial section; see, e.g., Woodward & Maina, 2005, 2008; Maina & Woodward, 2009; Woodward et al., 2021). Primary and secondary bronchi of select scans are almost entirely segmented by hand in the original scan plane and revised on orthogonal planes to ensure accuracy. In contrast, segmentation of mammalian lungs is made easier by their comparatively simple anatomy, and usually just requires a more general thresholding to label all of the gas-exchanging tissues.

In higher-resolution scans (<100 μm) of avian lungs, manual segmentation can become an immensely time-consuming process (sometimes >100 h) due to image size, detail, and the number of slices, encumbering both the speed of the “segmentor” and the software algorithms (e.g., region-growing) that are selectively employed with these image stacks. While segmentation of the larger bronchi can be somewhat expedited by selective use of interpolation, these mostly manual or user-driven approaches are prohibitively time-consuming for the many tortuous and interconnected parabronchi of most avian taxa (Figure 7c,d). Instead, the entire parabronchial network—both its air-filled conduits and associated soft tissues—are manually segmented and consolidated into a single label. Soft tissues can then be extracted from this “parabronchial chunk” label by thresholding the more radiodense soft tissues and deleting them from the label (termed here as “chunk segmentation”; Figure 4). Each bronchus is then manually segmented to join with the previously segmented bronchi. In many birds, the parabronchi are too small to segment, similar to the alveoli of a mammalian lung.

While a combination of semiautomated segmentation and time-consuming manual refinement remains the standard approach to 3D visualization of nonhuman vertebrate pulmonary anatomy, recent developments in

machine learning-based segmentation have the potential to substantially improve and expedite workflows. In particular, deep learning—a form of machine learning that uses layered artificial neural networks (Janiesch et al., 2021)—has been increasingly applied to biological and biomedical imaging data (e.g., Lee et al., 2017; Liu, Song, et al., 2021; Scadeng et al., 2020; Urakubo et al., 2019; Wang et al., 2018). In versions of deep learning-based segmentation, the user manually segments a representative subset of the total scan data, which serves as input to train a neural network model that, in turn, segments the remainder of the image stack. Their capacity for pattern recognition allows trained neural networks to accurately distinguish structures that have varying grayscale intensity values. Trained models can be applied to subsequent datasets and can be optimized with additional training data to maintain accuracy across datasets. Such approaches are now embedded in some imaging software. For example, a variety of customizable neural network-based segmentation tools are available in Dragonfly based on models developed with TensorFlow and Keras (Makovetsky et al., 2018). To our knowledge, these approaches have not yet been applied to segmentation of nonhuman vertebrate lungs, particularly those of nonmammalian species, and represent a promising avenue of methodological development.

6 | LUNG SEGMENTATION IN FUNCTIONAL, COMPARATIVE, AND EVOLUTIONARY MORPHOLOGY

Lung modeling and segmentation holds substantial promise as a method for addressing anatomical, functional, and experimental questions in evolutionary biology. Thresholded models of human lungs have been used to evaluate sexual dimorphism, ventilation kinematics, and overall shape variation (Torres-Tamayo et al., 2018; Werner et al., 2009), and manual segmentation has been used to visualize the parenchymal and air space volumes of the respiratory gas bladder in *Arapaima*, an air-breathing osteoglossomorph fish (Scadeng et al., 2020). Ponganis et al. (2015) used 3D models of the respiratory system in three species of live penguins to quantify how lung volume relates to dive capabilities and the mechanisms associated with avoidance of barotrauma. York et al. (2018) used similar methods to visualize the lower respiratory system of three species of geese and evaluate the relationship between lung morphology and respiration in species adapted to flying at high altitudes (i.e., conditions of natural hypoxia). In both of the avian

studies, the authors thresholded the respiratory systems of the birds, and manually separated the gas-exchanging lungs from the cranially and caudally positioned sacs for analysis (York et al., 2018).

More detailed model creation requires more intensive manual segmentation and interpolation, usually of the negative spaces within the lung such as the bronchial tree. Examples of this include segmentation of the crocodilian bronchial tree (Farmer & Sanders, 2010; Sanders & Farmer, 2012; Schachner et al., 2013; Schachner et al., 2021; Schachner et al., 2022), the savannah monitor lizard (*Varanus exanthematicus*) (Schachner et al., 2014), and the common snapping turtle (*Chelydra serpentina*) (Schachner et al., 2017), all of which required a combination of manual and automatic segmentation methods. These types of models facilitate evaluation of airflow patterns when combined with experimental analyses and can provide a high-fidelity comparative framework for generating hypotheses of homology between related taxa (Cieri et al., 2014; Schachner et al., 2014; Schachner et al., 2021). Complex avian lung models have been generated for the African gray parrot (*P. erithacus*) (Lawson et al., 2021) (Figure 7) and the ostrich (*Struthio camelus*) (Schachner et al., 2021), both of which required a hybridization of the methods described in the previous section. The *P. erithacus* model resulted in the first complete high-resolution 3D digital model of an avian gas-exchanging lung with the parabronchial network intact. While these methods are time consuming (often taking 100+ hours or more per specimen), they allow for the analysis of the respiratory system in situ. This is critical, particularly in birds where the pulmonary tissues variably invade a substantial portion of the postcranial skeleton (O'Connor, 2004). Dissection of pulmonary tissues necessitates removal and destruction of the lungs, whereas latex casting (e.g., Duncker, 1971) prevents observations of many of the internal relationships between the bronchial tree and other pulmonary and visceral organs.

In situ imaging and segmentation of inflated lungs is generally considered the standard for pulmonary modeling in sauropsids; however, scanning casts of bronchial trees is a common method for evaluating bronchial tree morphology in nonhuman mammals such as rats and monkeys (Carson et al., 2010; Corley et al., 2012). Due to the relatively inflexible anatomy of the mammalian bronchoalveolar tree, and the restriction of the lungs to the thoracic cavity by the muscular diaphragm, this method can be a reasonable choice if the specimen is deceased at the time of data collection. A substantial downside to consider when imaging casts is that none of the other pulmonary tissues can be included in the model: the lung surfaces, pulmonary vasculature, and the bronchial trees cannot be modeled in association with

any adjacent organs or skeletal tissues. Mammalian lungs can also be excised, and then scanned in high resolution and segmented in regions using a combination of manual and automated reconstructions, as has been done for a piglet (Bauer et al., 2012) and for numerous murine bronchial trees rendered in isolation as surface models to evaluate intraspecific variation (Glenny et al., 2020). The substantial variation observed within the different strains of laboratory mice by Glenny et al. (2020) is notable and suggests that the bronchoalveolar lung of mammals is much more structurally variable than is generally accepted and should be a focus of study for anatomists.

Segmented surface models can be turned into polygon meshes, facilitating computational fluid dynamic (CFD) modeling of pressures and airflow through the bronchial tree. This method is much more established for modeling airflow through the upper respiratory system of extinct and extant nonhuman vertebrates like dinosaurs, dogs, and primates (e.g., Bourke et al., 2014; Bourke et al., 2022; Craven et al., 2009; Smith et al., 2019), but has not been used as often to address questions of airflow patterns in the lower respiratory system of nonhuman vertebrates, particularly sauropsids. CFD has been used to model the inspiratory valve of ostriches in streamlined “muffler” style truncated models of the proximal regions of the bronchial tree (Maina et al., 2009). Approaches like these reduce the extreme complexity of the avian lung and facilitate focused evaluation of the mechanics of airflow associated with individual bronchi. Others have modeled the jetting style of unidirectional airflow patterns in iguanas (Cieri et al., 2014), and the more complex unidirectional airflow patterns in varanids (Cieri & Farmer, 2020). The latter represents the most complex CFD model of airflow to date in a nonmammalian lung, and has been validated by experimental measurements of flow in both living and deceased specimens (Schachner et al., 2014). High-resolution meshes have been generated from scans of casts from a Sprague Dawley rat and a Rhesus monkey and used for CFD analysis of airflow in the lower respiratory system (Corley et al., 2012). Sverdlova et al. (2013) used a 3D CFD model of the trachea of domestic fowl to evaluate flow velocity and heat transfer. The use of CFD to model airflow patterns in sauropsid lungs is an extremely promising avenue for future research, as very little is known about patterns of flow in the lungs of most of the major clades within Sauropsida (Cieri & Farmer, 2016). More recently, some of these pulmonary 3D models have been incorporated into virtual reality (VR) and augmented reality space by biologists for both studying vertebrate morphology as well as communicating these data as an immersive experience to students and the public (Cieri et al., 2021).

Digitization is an ongoing initiative to convert specimen data into a digitally accessible format, helping to democratize and expand specimen research for evolutionary and global change studies (Hedrick et al., 2020). The Open exploration of Vertebrate Diversity (oVert) initiative is an NSF ADBC-TCN that has aimed to generate CT scan data for 80% of vertebrate genera (Watkins-Colwell et al., 2018). This incredibly important initiative has propelled comparative morphological research forward. However, the vast majority of these scans are for bone and the next steps in specimen digitization using CT will be to examine soft tissues as well as negative spaces (such as lungs). Making lung models available via online repositories such as MorphoSource (www.morphosource.org) will be part of the next stage of specimen digitization and enable “extended specimen” research on bird lungs (e.g., Hardisty et al., 2022; Webster, 2017).

7 | SEGMENTATION OF LUNGS FOR CLINICAL PURPOSES

Lung segmentation and 3D printing have been particularly useful for surgical planning. Yoon et al. (2019) segmented the lungs of patients with primary lung adenocarcinoma, 3D printed the models, and evaluated the usefulness of these models for improving patient understanding during the informed consent process related to their impending surgery (tumor resection). Their data demonstrated that the models improved comprehension of both consent and the procedure (Yoon et al., 2019). In other case studies, difficult or rare pulmonary ailments have been addressed using segmentation and 3D printing (or just segmentation alone); these include relapsing polychondritis (Tam et al., 2013), tracheobronchomalacia (Morrison et al., 2015), tracheal repair after resection (Cheng et al., 2017), airway stenosis due to inoperable malignancy and a multitude of other reasons (Guibert et al., 2020; Shan et al., 2021); for a review see (Cheng et al., 2017). Another area where segmentation and 3D printing are becoming more important is in preoperative planning for the 20–30% of patients with anomalies in their tracheobronchial tree and pulmonary vasculature (Cory & Valentine, 1959; Fourdrain et al., 2017; Smelt et al., 2019). While segmentation is growing as an active area of use in medicine and clinical research, it has not been as commonly employed in a clinical setting for respiratory diseases due to physicians lacking the technical skillset required to build complex 3D models (Cheng et al., 2016).

Video-assisted thoracic surgery is a standard and well-established surgical technique for lobectomies and segmentectomies, particularly for various types of tumors

(Hagiwara et al., 2014). Numerous studies have shown that intraoperative use of 3D volume renderings generated from CT scans of the patient (usually with proprietary software) assist surgeons in performing safe resections of the lung, and aid in determining the surgical margins for segmentectomies (Hagiwara et al., 2014; Oizumi et al., 2011; Saji et al., 2013). Additionally, during the planning stages of tumor resection surgery, segmentation can be used to visualize the pulmonary vasculature, bronchial tree, and associated tumors. These customized segmented patient-specific models can then be manipulated and studied in VR space by surgeons, thus helping to safeguard critical vasculature (Ujiie et al., 2021). Preoperative and even intraoperative segmentation has been used to generate models of the heart and vasculature to safely plan and execute surgical intervention for rare congenital heart malformations (e.g., pulmonary artery atresia with ventricular septal defect and major aortopulmonary collateral arteries) (Cen et al., 2021). Preoperative and intraoperative segmentation has also been used to render models of the cardiopulmonary system of conjoined twins during surgical separation (Juhnke et al., 2019). More recently, segmented models of the lungs of smokers were used to teach children about the dangers of smoking via augmented reality (Borovanska et al., 2020).

Segmentation of the lower respiratory system is less often used for veterinary clinical research and medicine; however, there has been some ground-breaking work using these methods on animals. Li et al. (2014) generated 3D segmented models of canine lungs as a biomimetic prosthesis to reduce life-threatening complications from postoperative transplantation after a pneumonectomy. The 3D printed lung models were surgically implanted into the empty half of the thoracic cavity with the aim of reducing postoperative movement of the mediastinum and surgical complications after the removal of a lung, a highly risky procedure that is often necessary with lung cancer, thoracic trauma, bronchiectasis, and other severe ailments (Li et al., 2014; Riquet et al., 2013). Segmented models of the feline respiratory system were used by Dillon et al. (2014) to visually demonstrate the impact of heartworms (*Dirofilaria immitis*) on cardiopulmonary tissues relative to those of healthy cats in tandem with histopathology, radiographs, and numerous other methods.

Automated pulmonary segmentation of CT data with deep learning has led to numerous additional clinical applications such as general lung lobe segmentation (Park et al., 2020) and segmentation for radiotherapy treatment planning (Liu, Li, et al., 2021). Deep learning-based segmentation has also been applied to a variety of complex lung pathology such as cases of cryptogenic organizing pneumonia, usual interstitial pneumonia, and nonspecific

interstitial pneumonia (Park et al., 2019). Additionally, multiple AI-driven segmentation approaches have been utilized in the setting of the COVID-19 pandemic (Aiello et al., 2022; Gholamiankhah et al., 2022). For a review of automated lung segmentation, see Carmo et al. (2022).

8 | THE IMPACT OF COVID-19 ON THE RESPIRATORY SYSTEM: VISUALIZING DISEASE

Recent radiologic literature has given considerable attention to the atypical pneumonia associated with coronavirus disease 2019 (COVID-19), a complication resulting from infection with severe acute respiratory syndrome coronavirus 2 (SARS-CoV2). While the routine use of CT in the diagnosis of COVID-19 has been discouraged by leaders in the field of radiology (Rubin et al., 2020; Simpson et al., 2020), CT has persisted as a focal point of discussion around its use as a supplemental tool for the diagnosis of COVID-19 pneumonia (Waller et al., 2020). Distinctive CT patterns have been described in affected patients with the prevailing theme being that of bilateral “patchy” or “confluent, band-like” ground glass opacity or consolidation in a peripheral and mid-to-lower lung zone distribution (Bai et al., 2020; Bernheim et al., 2020; Cheng et al., 2020; Chung et al., 2020; Guan et al., 2020; Han et al., 2020; Li et al., 2020; Rubin et al., 2020; Simpson et al., 2020; Wei et al., 2020; Ye et al., 2020; Zhao et al., 2020; Zhou et al., 2020). The presence of these typical CT findings common for COVID-19 in conjunction with the appropriate clinical suspicion for COVID-19 can have an impact on patient care, for example, when reverse-transcription polymerase chain reaction (RT-PCR) tests are negative for SARS-CoV2. Segmentation of models facilitates communication with patients (Yoon et al., 2019), and may aid in the diagnosis of complex respiratory infections, particularly if these diseases occupy the pleural spaces and parenchyma in a specific, diagnostic manner not easily identified via radiograph or CT.

To demonstrate the utility of lung segmentation on COVID-19, we conducted a condensed clinical study on seven individuals who were admitted to University Medical Center (UMC) in New Orleans presenting with symptoms of COVID-19 during the first year of the pandemic. Two of the individuals tested negative but were identified by their attending physicians as false negatives due to the presentation of concerning symptoms including shortness of breath and fever. To provide a control group, scans were obtained from five individuals who were scanned for reasons unrelated to COVID-19 and who did not have COVID-19. The LSUHSC institutional review board approved this retrospective study with

TABLE 2 Characteristics of the patients involved in this study. In some individuals, BMI was not indicated in their chart and weight was reported in parentheses (in lbs.)

Patient ID	Age	Sex	Height (m)	BMI	COVID	Ventilator (Y/N)	Comorbidities	Time from onset of symptoms to scan (days)	Total length of stay
1	56	M	1.702	32.39	False negative	N	Smoking and hypertension	10	7
2	55	F	1.651	35.01	Positive	N	DM2, HTN, breast cancer s/p chemo	21	7
3	50	M	1.778	31.57	Negative	N	HTN, smoking	10	
4	39	F	1.651	49.65	Positive	N	HTN, prediabetes	4	13
5	46	M	1.803	24.3	Positive	N	DM2, hypertrophic CM, CAD	2	6
6	61	F	1.626	30.9	Positive	Y	DM2, HTN	7	16
7	57	F	1.626	42.29	False negative	N	Former smoker, obesity, DM2, HTN, HLD		
8	70	M	1.727	(210)	Negative	N	Sternal surgery	N/A	N/A
9	26	F	1.702	20.36	Negative	N	N/A	N/A	N/A
10	53	M	1.778	(240)	Negative	N	N/A	N/A	N/A
11	28	M	1.829	(195)	Negative	N	N/A	N/A	N/A
12	55	F	1.524	35.15	Positive	N	N/A	N/A	N/A

Abbreviations: CAD, coronary artery disease; CM, cardiomyopathy; DM2, type II diabetes; HLD, hyperlipidemia; HTN, hypertension.

waiver of Health Insurance Portability and Accountability Act authorization in accordance with federal regulations at 45 CFR 164.512 (i) (2) (ii). We performed a database query within the electronic medical record system at LSUHSC for all patients who had undergone COVID-19 RT-PCR assay in association with the Louisiana Office of Public Health. The thoracic CTs were performed either for worsening respiratory symptoms or suspicion for pulmonary embolus (PE). All CT examinations were obtained using a Philips iCT 256 CT system (Koninklijke Philips N.V., Amsterdam, Netherlands). Data were acquired using a 128×0.625 mm detector configuration with dual sampling or 64×0.625 mm detector configuration with dual sampling, rotation time of 0.33 s, tube voltage of 120 kVp, and reference tube current of 72 mAs with dose modulation. All CTs at LSUHSC were performed after 1.5 ml/kg of non-ionic intravenous contrast material (iohexol, Omnipaque 350 mg/100 ml, GE Healthcare, Chicago, IL) was injected via an 18–20-gauge (G) catheter (18 G for PE studies and 20 G for routine) inserted in an antecubital vein at a rate of 2–3 ml/s using a power injector (MEDRAD Stellant FLEX, Whippany, NJ). Images were reformatted as 2.5 mm thick sections (with 0.9 mm thin sections on PE protocols) with no overlap and sent to a PACS workstation.

We merged threshold-based segmentation with manual (user-driven) segmentation to produce six 3D, multi-layered surface models of the respiratory system. These individuals range from a diagnosis of normal to severe COVID-19 disease (Tables 2 and 3). The models were segmented in Avizo 7.1 (Thermo Fisher Scientific) with a Wacom Intuos Pro pen tablet. These multilayered models facilitate the visualization of disease throughout the lungs in relation to the thorax (Figure 8a,e), as a transparent material in relation to the bronchial tree (Figure 8b–d), and as a solid in relation to the unaffected parenchyma (Figure 8f). The models also facilitate demonstration of visual differentiation between normal, mild, moderate, and severe disease, a false negative, and severe case with acute respiratory distress syndrome in relation to the CT cross sections (Figures 9 and 10). Translation of the 2D axial and coronal cross-sections to the 3D surface models can be extremely effective for communication of pulmonary data to students, educators, clinicians, and, importantly, the general public (Ho et al., 2019). This can be critical during a public health crisis like the COVID-19 pandemic (Kabir et al., 2021; Schachner & Spieler, 2020). This can be used to quantify lung volumes, including asymmetry (Table 3), and track volumes of organs or tumors over time. While sometimes more time-consuming to create than the AI-segmented models, these combined

TABLE 3 Pulmonary measures derived from the segmented CT-based models. Lung volumes are in liters.

ID	CT comments	Left lung volume (total)	Right lung volume (total)	Left healthy lung volume	Right healthy lung volume	Left lung GGO/C	Right lung GGO/C	Left lung ARDS	Right lung ARDS	Left total infection	Right total infection
1	Severe (false negative)	1.24	1.71	0.84	0.87	0.41	0.84	0.00	0.00	0.41	0.84
2	Classic COVID, severe w ARDS	1.17	1.45	0.05	0.03	0.10	0.24	1.00	1.18	1.10	1.42
3	Normal, PUI	3.20	3.62	3.20	3.62	0.00	0.00	0.00	0.00	0.00	0.00
4	Classic COVID, mild	0.87	1.15	0.68	0.94	0.18	0.21	0.00	0.00	0.18	0.21
5	Classic COVID, mild	1.51	1.79	1.42	1.71	0.09	0.08	0.00	0.00	0.09	0.08
6	Classic COVID, severe	0.87	0.90	0.61	0.52	0.26	0.38	0.00	0.00	0.26	0.38
7	Classic COVID, moderate	0.87	1.08	0.66	0.93	0.21	0.16	0.00	0.00	0.21	0.16
8	Normal	1.89	2.34	1.89	2.34	0.00	0.00	0.00	0.00	0.00	0.00
9	Normal	0.92	1.31	0.92	1.31	0.00	0.00	0.00	0.00	0.00	0.00
10	Normal	2.40	2.99	2.40	2.99	0.00	0.00	0.00	0.00	0.00	0.00
11	Normal	1.45	1.69	1.45	1.69	0.00	0.00	0.00	0.00	0.00	0.00
12	Mild	0.89	0.94	0.89	0.76	0.00	0.19	0.00	0.00	0.00	0.19

Abbreviations: ARDS, acute respiratory distress syndrome; C, consolidated infection; CT, computed tomography; GGO, ground glass opacities; PUI, persons under investigation (for COVID-19).

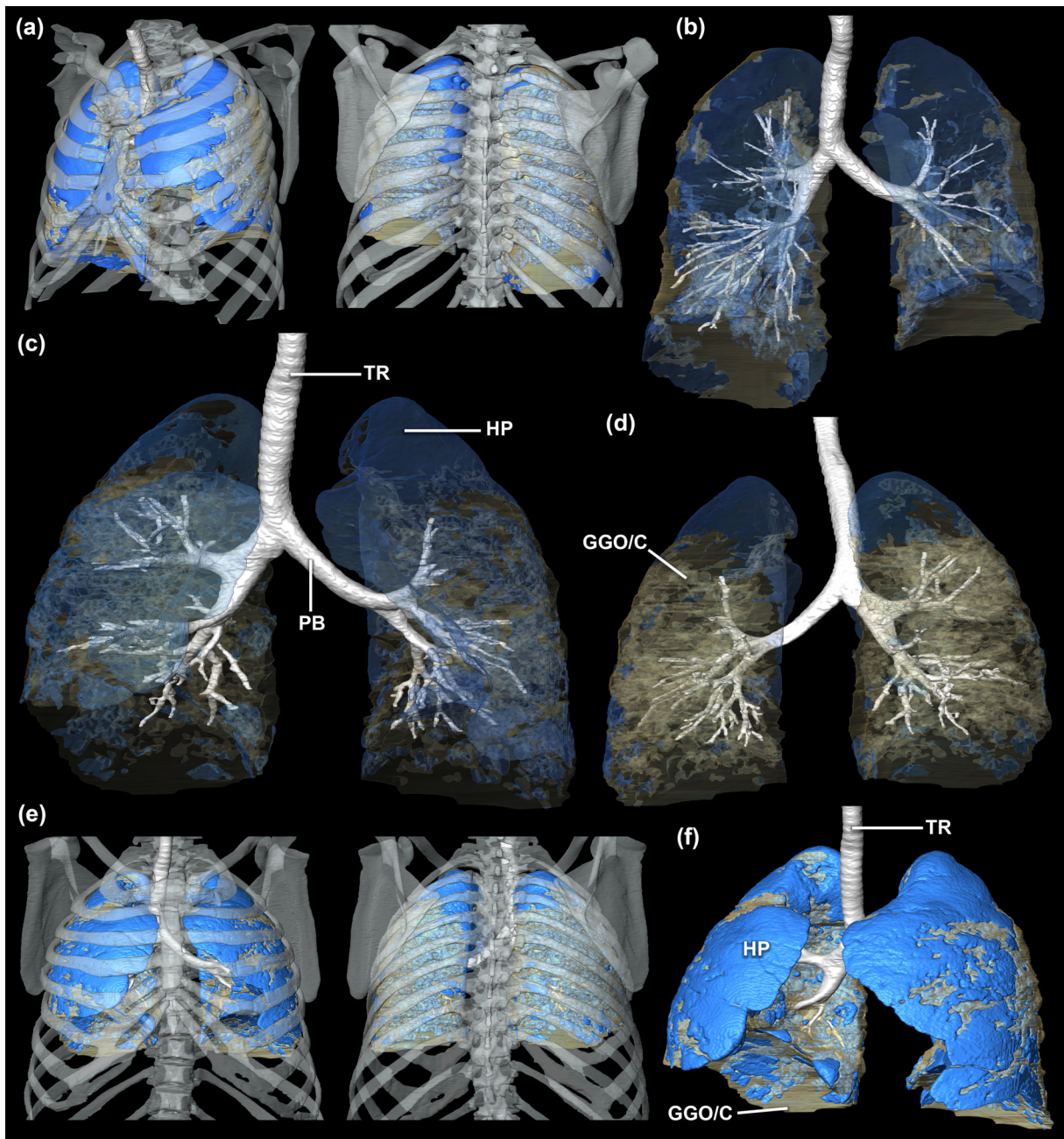


FIGURE 8 Segmented surface model of the skeleton, bronchial tree, and lungs of Patients 1 and 6 (see Table 1 for patient characteristics). Healthy/normal parenchyma is represented as solid or transparent blue, diseased lung tissue is a semitransparent yellow. (a) Skeletal and pulmonary model of Patient 1 in left anterolateral (left) and posterior (right) views. (b) Translucent lung model of Patient 1 in anterior view with the bronchial tree represented as a solid. Translucent lung model of Patient 6 in anterior view (c) and in posterior view (d) with the bronchial tree represented as a solid. Model of Patient 6 with the healthy/normal parenchyma represented as a solid in anterior (e) and posterior views (e, right) with the skeleton present, and in left craniolateral view (f). GGO/C, ground glass opacities/consolidation; HP, healthy parenchyma; PB, primary bronchus; TR, trachea.

thresholded/manually segmented models fill an important separate niche within imaging based-medicine, providing a more detailed and accurate model for individualized medicine such as tumor tracking or communicating disease impact with the public.

9 | FUTURE DIRECTIONS

AI segmentation is a massive and growing field for the visualization of organ systems from CT data, particularly for the respiratory system in humans (for a review of

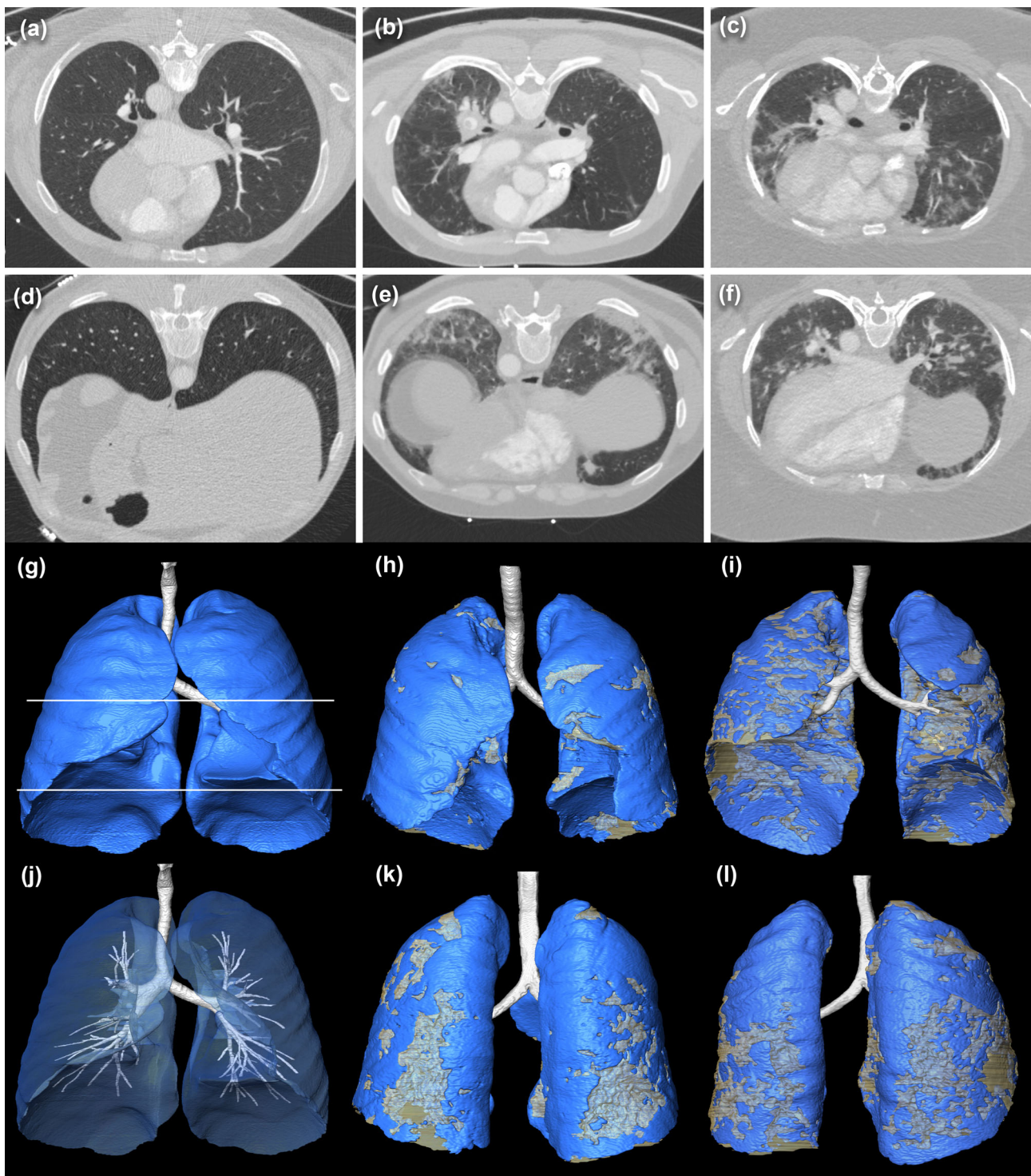


FIGURE 9 Axial slices through computed tomography (CT) scans of patients with varying respiratory states (normal/control to moderate pulmonary disease resulting from COVID-19) and the associated segmented surface models. Horizontal white lines in (g) demonstrate the approximate locations of the slices in each of the models. Patient 3 (normal/control) axial slices (a, d), and models (g, j) in anterior view (j demonstrates the bronchial tree with the parenchyma made translucent). Patient 5 (mild disease) axial slices (b, e), and models in anterior (h) and posterior (k) views. Patient 4 (moderate disease) axial slices (c, f), and models in anterior (i) and posterior (l) views. Blue represents unaffected parenchyma; yellow represents the ground-glass opacities/consolidation.

pulmonary lobe segmentation see Doel et al., 2015). The American Association of Physicists in Medicine (AAPM) recently held a two-year long open competition, the

AAPM Thoracic Auto-segmentation Challenge, to provide a platform to evaluate the best methods for CT segmentation of the lungs and other thoracic organs in

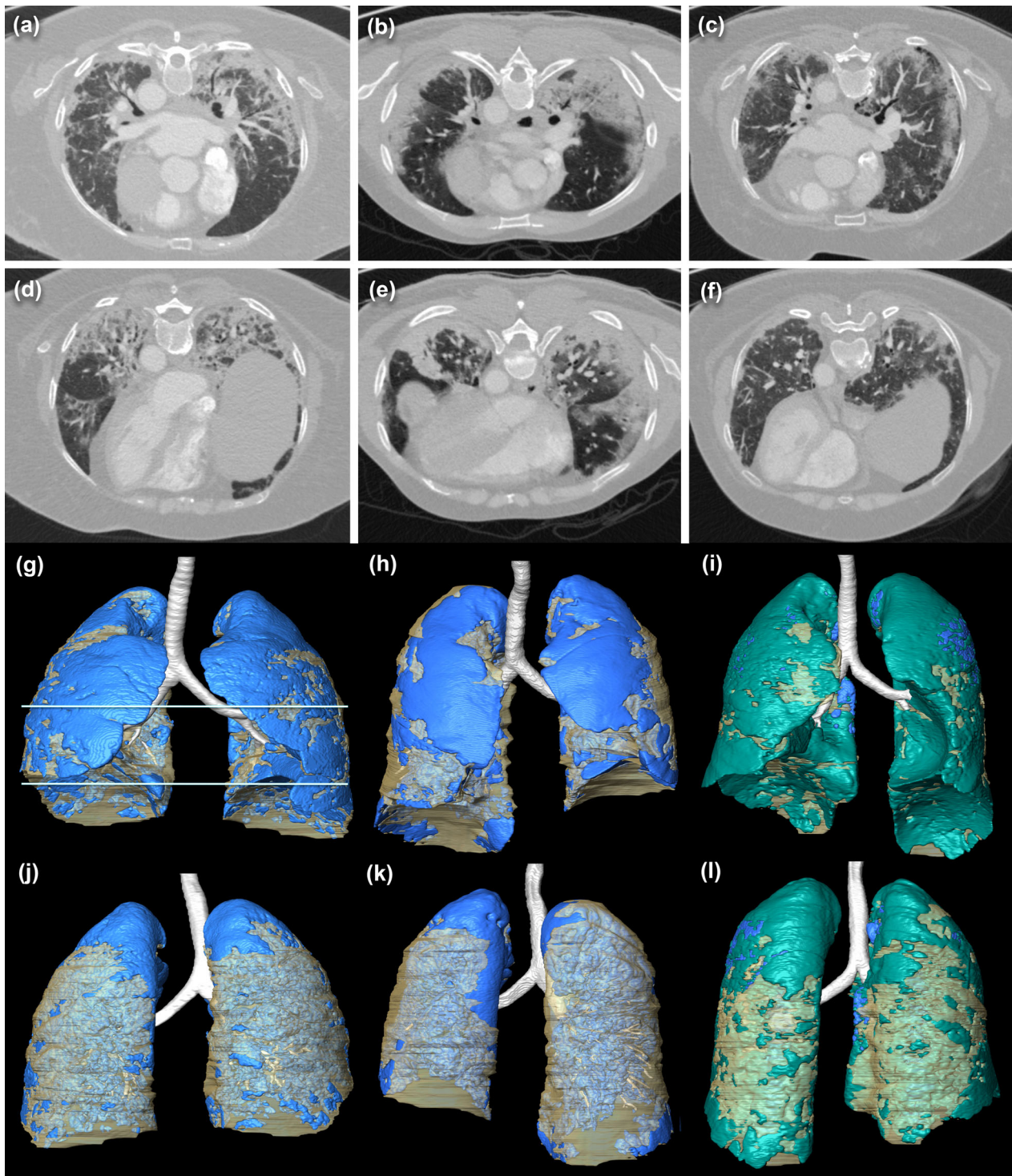


FIGURE 10 Axial slices through computed tomography (CT) scans of patient lungs with varying respiratory states (normal/control to moderate pulmonary disease) with COVID-19 and the associated segmented surface models. Horizontal white lines in (g) demonstrate the approximate locations of the slices in each of the models. Patient 6 (severe disease) axial slices (a, d), and models in anterior (g) and posterior (j) views. Patient 1 (severe disease/false negative) CT axial slices (b, e), and models in anterior (h) and posterior (k) views. Patient 11 (severe disease/acute respiratory distress syndrome [ARDS]) axial slices (c, f), and models in anterior (i) and posterior (l) views. Blue represents unaffected parenchyma; yellow represents the ground glass opacities/consolidation; green, represents ARDS.

humans (<http://aapmchallenges.cloudapp.net/competitions/3>). This field is growing particularly because of the COVID-19 pandemic. For example, a team recently used

deep learning algorithms to detect the presence of COVID-19 pneumonia with up to 84% sensitivity and 93% specificity (Harmon et al., 2020). While there have

been substantial efforts dedicated to algorithms for lung segmentation in human pulmonary research, to our knowledge there has been little to no work in this area on nonmammalian amniotes. More communication between the basic sciences and clinicians who work on lung imaging would substantially benefit the field of lung biology and imaging particularly as the methods used to study the respiratory system are applicable across species supporting the One Health initiative. Additionally, respiratory pathologies like avian flu are an annual problem, and collaborations between clinicians and basic scientists interested in lung biology outside of the mammalian respiratory system would have the potential to benefit the public as well as researchers interested in questions on sauropsid lung evolution, anatomy, and function.

Considering that most 3D anatomical modeling in nonhuman vertebrates has been done on heads, skeletons, and limbs, more models are needed to evaluate the interface between the respiratory system and adjacent tissues, like cardiovascular and gastrointestinal systems. Finite element models evaluating lung motion during ventilation in humans show substantial promise (Werner et al., 2009); however, these studies are difficult to validate experimentally, and this remains a wide-open area of investigation for all other air-breathing vertebrates. Additionally, CFD modeling of airflow patterns in the tracheobronchial tree of a broader range of air-breathing taxa will elucidate the divergent evolutionary ventilatory strategies within amniotes, particularly the origin of unidirectional airflow patterns within Sauropsida and tidal flow patterns along the ancestral mammalian line.

AUTHOR CONTRIBUTIONS

Emma R Schachner: Conceptualization; data curation; formal analysis; funding acquisition; investigation; methodology; project administration; resources; software; supervision; validation; visualization; writing – original draft; writing – review and editing. **Adam B. Lawson:** Conceptualization; formal analysis; methodology; visualization; writing – original draft; writing – review and editing. **Aracely Martinez:** Visualization; writing – original draft; writing – review and editing. **Clinton A. Grand Pre:** Visualization; writing – original draft; writing – review and editing. **Carl Sabottke:** Writing – original draft; writing – review and editing. **Farid Abou-Issa:** Writing – original draft; writing – review and editing. **Scott Echols:** Data curation; formal analysis; investigation; methodology; resources; visualization; writing – original draft; writing – review and editing. **Raul E. Diaz Jr.:** Resources; writing – original draft; writing – review and editing. **Andrew J. Moore:** Writing – original draft; writing – review and editing. **John-Paul Grenier:** Data curation;

resources; writing – original draft; writing – review and editing. **Brandon P. Hedrick:** Formal analysis; funding acquisition; methodology; resources; writing – original draft; writing – review and editing. **Bradley Spieler:** Conceptualization; data curation; formal analysis; investigation; methodology; project administration; resources; supervision; validation; writing – original draft; writing – review and editing.

ACKNOWLEDGMENTS

The authors thank the anonymous patients whose imaging data were included in this manuscript. The authors thank the two anonymous reviewers and the editor who substantially improved this manuscript. The authors also thank the imaging technicians at UMC in New Orleans for their hard work during the COVID-19 pandemic, the imaging team at Parrish Creek Veterinary Hospital and Diagnostic Center, UT, Tautis Skorka at the Molecular Imaging Center at the University of Southern California, and Chris Clark (UC Riverside) for access to specimens for a project tangential to this study. Special thanks to CP Layton for assistance with Adobe Photoshop. This work was funded in part by a Louisiana State University Health Sciences Research Enhancement Program Grant to ERS and BPH. Images of specimens included in this review were obtained for projects distinct from this study; however, they were covered by an IACUC to ERS at LSUHSC (#T3368) or were imaged for clinical purposes entirely unrelated to this research.

FUNDING INFORMATION

This work was funded in part by a Louisiana State University Health Sciences Research Enhancement Program Grant to ERS and BPH.

CONFLICT OF INTEREST

The authors declare no conflict of interest.

ORCID


Emma R. Schachner  <https://orcid.org/0000-0002-8636-925X>

Adam B. Lawson  <https://orcid.org/0000-0001-6088-159X>

Aracely Martinez  <https://orcid.org/0009-0005-2888-6434>

Clinton A. Grand Pre  <https://orcid.org/0009-0000-3823-8362>

Raul E. Diaz Jr  <https://orcid.org/0000-0001-9107-124X>

Andrew J. Moore  <https://orcid.org/0000-0002-3023-2502>

Brandon P. Hedrick  <https://orcid.org/0000-0003-4446-3405>

Bradley Spieler  <https://orcid.org/0000-0002-7346-2885>

REFERENCES

- Aiello, M., Baldi, D., Esposito, G., Valentino, M., Randon, M., Salvatore, M., & Cavaliere, C. (2022). Evaluation of AI-based segmentation tools for COVID-19 lung lesions on conventional and ultra-low dose CT scans. *Dose-Response*, 20, 15593258221082896.
- Aslanidi, O. V., Colman, M. A., Zhao, J., Smaill, B. H., Gilbert, S. H., Hancox, J. C., Boyett, M. R., & Zhang, H. (2012). Arrhythmogenic substrate for atrial fibrillation: Insights from an integrative computation model of pulmonary veins. 34th Annual International Conference of the IEEE Engineering in Medicine and Biology Society. 28:203-206.
- Asorey, I., L. P., Canfrán, S., Ortiz-Díez, G., & Aguado, D. (2020). Factors affecting respiratory system compliance in anaesthetised mechanically ventilated healthy dogs: A retrospective study. *Journal of Small Animal Practice*, 61, 617–623.
- Bai, H. X., Hsieh, B., Xiong, Z., Halsey, K., Choi, J. W., Tran, T. M. L., Pan, I., Shi, L.-B., Wang, D.-C., Mei, J., Jiang, X.-L., Zeng, Q.-H., Egglin, T. K., Hu, P.-F., Agarwal, S., Xie, F., Li, S., Healey, T., Atalay, M. K., & Liao, W.-H. (2020). Performance of radiologists in differentiating COVID-19 from viral pneumonia on chest CT. *Radiology*, 296, 200823.
- Bauer, C., Adam, R., Stoltz, D. A., & Beichel, R. R. (2012). Computer-aided analysis of airway trees in micro-CT scans of ex vivo porcine lung tissue. *Computerized Medical Imaging and Graphics*, 36, 601–609.
- Bernheim, A., Mei, X., Huang, M., Yang, Y., Fayad, Z. A., Zhang, N., Diao, K., Lin, B., Zhu, X., Li, K., Li, S., Shan, H., Jacobi, A., & Chung, M. (2020). Chest CT findings in coronavirus disease-19 (COVID-19): Relationship to duration of infection. *Radiology*, 295, 200463.
- Bhalla, A. S., Das, A., Naranje, P., Irodi, A., Raj, V., & Goyal, A. (2019). Imaging protocols for CT chest: A recommendation. *Indian Journal of Radiology and Imaging*, 29, 236–246.
- Booz, C., Vogl, T. J., Schoepf, U. J., Caruso, D., Inserra, M. C., Yel, I., Martin, S. S., Bucher, A. M., Lenga, L., Caudo, D., Schreckenbach, T., Schoell, N., Huegel, C., Stratmann, J., Vasa-Nicotera, M., Rachovitsky-Duarte, D. E., Laghi, A., De Santis, D., Mazziotti, S., ... Albrecht, M. H. (2021). Value of minimum intensity projections for chest CT in COVID-19 patients. *European Journal of Radiology*, 135, 109478.
- Borovanska, Z., Poyade, M., Rea, P. M., & Buksh, I. D. (2020). Engaging with children using augmented reality on clothing to prevent them from smoking. In: *Advances in Experimental Medicine and Biology*, book series. S *Biomedical visualization* (Vol. 1262, pp. 59–94).
- Bourke, J. M., Fontenot, N., & Holliday, C. M. (2022). Septal deviation in the nose of the longest faced crocodylian: A description of nasal anatomy and airflow in the Indian gharial (*Gavialis gangeticus*) with comments on acoustics. *The Anatomical Record*, 305, 2883–2903.
- Bourke, J. M., Porter, W. R., Ridgely, R. C., Lyson, T. R., Schachner, E. R., Bell, P. R., & Witmer, L. M. (2014). Breathing life into dinosaurs: Tackling challenges of soft-tissue restoration and nasal airflow in extinct species. *The Anatomical Record*, 297, 2148–2186.
- Carmo, D., Ribeiro, J., Dertkigil, S., Appenzeller, S., Lotufo, R., & Rittner, L. (2022). A systematic review of automated segmentation methods and public datasets for the lung and its lobes and findings on computed tomography images. *Yearbook of Medical Informatics*, 31, 277–295.
- Carson, J. P., Einstein, D. R., Minard, K. R., Fanucchi, M. V., Wallis, C. D., & Corley, R. A. (2010). High resolution lung airway cast segmentation with proper topology suitable for computational fluid dynamic simulations. *Computerized Medical Imaging and Graphics*, 34, 572–578.
- Cen, J., Liufu, R., Wen, S., Qiu, H., Liu, X., Chen, X., Yuan, H., Huang, M., & Zhuang, J. (2021). Three-dimensional printing, virtual reality and mixed reality for pulmonary atresia: Early surgical outcomes evaluation. *Heart, Lung and Circulation*, 30, 296–302.
- Cheng, G. Z., Estepar, R. S. J., Folch, E., Onieva, J., Gangadharan, S., & Majid, A. (2016). Three-dimensional printing and 3D-slicer: Powerful tools in understanding and treating structural lung disease. *Chest*, 149, 1136–1142.
- Cheng, G. Z., Folch, E., Wilson, A., Brik, R., Garcia, N., Estepar, R. S. J., Onieva, J. O., Gangadharan, S., & Majid, A. (2017). 3D printing and personalized airway stents. *Pulmonary Therapy*, 3, 59–66.
- Cheng, Z., Lu, Y., Cao, Q., Qin, L., Pan, Z., Yan, F., & Yang, W. (2020). Clinical features and chest CT manifestations of coronavirus disease 2019 (COVID-19) in a single-center study in Shanghai, China. *American Journal of Roentgenology*, 215, 121–126.
- Chung, M., Bernheim, A., Mei, X., Zhang, N., Huang, M., Zeng, X., Cui, J., Xu, W., Yang, Y., Fayad, Z. A., Jacobi, A., Li, K., Li, S., & Shan, H. (2020). CT imaging features of 2019 novel coronavirus (2019-nCoV). *Radiology*, 295, 202–207.
- Cieri, R. L., Crave, B. A., Schachner, E. R., & Farmer, C. G. (2014). New insight into the evolution of the vertebrate respiratory system and the discovery of unidirectional airflow in iguana lungs. *Proceedings of the National Academy of Sciences of the United States of America*, 111, 17218–17223.
- Cieri, R. L., & Farmer, C. G. (2016). Unidirectional pulmonary airflow in vertebrates: A review of structure, function, and evolution. *Journal of Comparative Physiology B*, 186, 541–552.
- Cieri, R. L., & Farmer, C. G. (2020). Computational fluid dynamics reveals a unique net unidirectional pattern of pulmonary airflow in the savannah monitor lizard (*Varanus exanthematicus*). *The Anatomical Record*, 303, 1768–1791.
- Cieri, R. L., Turner, M. L., Carney, R. M., Falkingham, P. L., Kirk, A. M., Wang, T., Jensen, B., Novotny, J., Tveite, J., Gatesy, S. M., Laidlaw, D. H., Kaplan, H., Moorman, A. F. M., Howell, H., Engel, B., Cruz, C., Smith, A., Gerichs, W., Lian, Y., ... Farmer, C. G. (2021). Virtual and augmented reality: New tools for visualizing, analyzing, and communicating complex morphology. *Journal of Morphology*, 282, 1785–1800.
- Corley, R. A., Kabilan, S., Kuprat, A. P., Carson, J. P., Minard, K. R., Jacob, R. E., Timchalk, C., Glenny, R., Pipavath, S., Cox, T., Wallis, C. D., Larson, R. F., Fanucchi, M. V., Postlethwait, E. M., & Einstein, D. R. (2012). Comparative computational modeling of airflows and vapor dosimetry in the respiratory tracts of rat, monkey, and human. *Toxicological Sciences*, 128, 500–516.
- Cory, R. A. S., & Valentine, E. J. (1959). Varying patterns of the lobar branches of the pulmonary artery. *Thorax*, 14, 267–280.

- Craven, B. A., Paterson, E. G., Settles, G. S., & Lawson, M. J. (2009). Development and verification of a high-fidelity computational fluid dynamics model of canine nasal airflow. *Journal of Biomechanical Engineering*, *131*, 091002.
- Dillon, A. R., Tillson, D. M., Wooldridge, A., Cattley, R., Hathcock, J., Brawner, W. R., Cole, R., Welles, B., Christopherson, P. W., Lee-Fowler, T., Bordelon, S., Barney, S., Sermersheim, M., Garbarino, R., Wells, S. Z., Diffie, E. B., & Schachner, E. R. (2014). Effect of pre-cardiac and adult stages of *Dirofilaria immitis* in pulmonary disease of cats: CBC, bronchial lavage cytology, serology, radiographs, CT images, bronchial reactivity, and histopathology. *Veterinary Parasitology*, *206*, 24–37.
- Doel, T., Gavaghan, D. J., & Grau, V. (2015). Review of automatic pulmonary lobe segmentation methods from CT. *Computerized Medical Imaging and Graphics*, *40*, 13–29.
- Drebin, R. A., Carpenter, L., & Hanrahan, P. (1988). Volume rendering. *Computer Graphics*, *22*, 65–74.
- Driggers, T. (2000). Respiratory diseases, diagnostics, and therapy in snakes. *Respiratory Medicine*, *3*, 519–530.
- Duncker, H. R. (1971). The lung air sac system of birds. A contribution to the functional anatomy of the respiratory apparatus. *Ergebnisse der Anatomie und Entwicklungsgeschichte*, *45*, 1–171.
- Escobar, A., da Rocha, R. W., Pypendop, B. H., Filho, D. Z., Sousa, S. S., & Valadão, C. A. A. (2016). Effects of methadone on the minimum anesthetic concentration of isoflurane, and its effects on heart rate, blood pressure and ventilation during isoflurane anesthesia in hens (*Gallus gallus domesticus*). *PLoS One*, *11*, e0152546.
- Farmer, C. G. (2017). Pulmonary transformations in vertebrates. In J. N. Maina (Ed.), *The biology of the avian respiratory system* (pp. 99–112). Springer Cham.
- Farmer, C. G. (2021). Linking structure and function in the vertebrate respiratory system: A tribute to August Krogh. *Comparative Biochemistry and Physiology, Part A*, *255*, 110892.
- Farmer, C. G., & Sanders, K. (2010). Unidirectional airflow in the lungs of alligators. *Science*, *327*, 338–340.
- Fedorov, A., Beichel, R., Kalpathy-Cramer, J., Finet, J., Fillion-Robin, J.-C., Pujol, S., Bauer, C., Jennings, D., Fennessy, F. M., Sonka, M., Buatti, J., Aylward, S. R., Miller, J. V., Pieper, S., & Kikinis, R. (2012). 3D slicer as an image computing platform for the quantitative Imaging network. *Magnetic Resonance Imaging*, *30*, 1323–1341.
- Fourdrain, A., De Dominicis, F., Blanchard, C., Iquille, J., Lafitte, S., Beuvry, P.-L., Michel, D., Merlusca, G., Havet, E., & Berna, P. (2017). Three-dimensional CT angiography of anatomic variations in the pulmonary arterial tree. *Surgical and Radiologic Anatomy*, *40*, 45–53.
- García-Sanz, V., Canfrán, S., Gómez de Segura, I. A., & Aguado, D. (2020). Effect of recumbency and body condition score on open-lung positive end-expiratory pressure and respiratory system compliance following a stepwise lung recruitment manoeuvre in healthy dogs during general anaesthesia. *Research in Veterinary Science*, *132*, 177–185.
- George, I. D., & Holliday, C. M. (2013). Trigeminal nerve morphology in *Alligator mississippiensis* and its significance for crocodyliform facial sensation and evolution. *The Anatomical Record*, *296*, 670–680.
- Gholamiankhah, F., Mostafapour, S., Abdi Goushbolagh, N., Shojaerazavi, S., Layegh, P., Tabatabaei, S. M., & Arabi, H. (2022). Automated lung segmentation from computed tomography images of normal and COVID-19 pneumonia patients. *Iranian Journal of Medical Sciences*, *47*, 440–449.
- Gignac, P. M., & Kley, N. J. (2018). The utility of DiceCT imaging for high-throughput comparative neuroanatomical studies. *Brain, Behavior and Evolution*, *91*, 180–190.
- Gignac, P. M., Kley, N. J., Clarke, J. A., Colbert, M. W., Morhardt, A. C., Cerio, D., Cost, I. N., Cox, P. G., Daza, J. D., Early, C. M., Echols, S., Henkelman, R. M., Herdina, A. N., Holliday, C. M., Li, Z., Mahlow, K., Merchant, S., Müller, J., Osborn, C. P., ... Witmer, L. M. (2016). Diffusible iodine-based contrast-enhanced computed tomography (diceCT): An emerging tool for rapid, high-resolution, 3-D imaging of metazoan soft tissues. *Journal of Anatomy*, *228*, 889–909.
- Glenny, R. W., Krueger, M., Bauer, C., & Beichel, R. R. (2020). The fractal geometry of bronchial trees differs by strain in mice. *Journal of Applied Physiology*, *128*, 362–367.
- Guan, W., Liu, J., & Yu, C. (2020). CT findings of coronavirus disease (COVID-19) severe pneumonia. *American Journal of Roentgenology*, *214*, W85–W86.
- Guibert, N., Saka, H., & Dutau, H. (2020). Airway stenting: Technological advancements and its role in interventional pulmonology. *Respirology*, *25*, 953–962.
- Gumpfenberger, M. (2021). Diagnostic imaging of the respiratory tract of the reptile patient. *Veterinary Clinics of North America: Exotic Animal Practice*, *24*, 293–320.
- Hagiwara, M., Shimada, Y., Kato, Y., Nawa, K., Makino, Y., Furumoto, H., Akata, S., Kakihana, M., Kajiwara, N., Ohira, T., Saji, H., & Ikeda, N. (2014). High-quality 3-dimensional image simulation for pulmonary lobectomy and segmentectomy: Results of preoperative assessment of pulmonary vessels and short-term surgical outcomes in consecutive patients undergoing video-assisted thoracic surgery. *European Journal of Cardio-Thoracic Surgery*, *46*, e120–e126.
- Hall, R., Mutumi, G., Hedrick, B. P., Dávalos, L. M., Rossiter, S., Sears, K., & Dumonat, E. R. (2021). Find the food first: An omnivorous sensory morphotype predates biomechanical specialization for plant based diets in phyllostomid bats. *Evolution*, *75*, 2791–2801.
- Han, R., Huang, L., Jiang, H., Dong, J., Peng, H., & Zhang, D. (2020). Early clinical and CT manifestations of coronavirus disease 2019 (COVID-19) pneumonia. *American Journal of Roentgenology*, *215*, 338–343.
- Hardisty, A. R., Ellwood, E. R., Nelson, G., Zimkus, B., Buschbom, J., Addink, W., Rabeler, R. K., Bates, J., Bentley, A., Fortes, J. A. B., Hansen, S., Macklin, J. A., Mast, A. R., Miller, J. T., Monfils, A. K., Paul, D. L., Wallis, E., & Webster, M. (2022). Digital extended specimens: Enabling an extensible network of biodiversity data records as integrated digital objects on the internet. *Bioscience*, *72*, 978–987.
- Harmon, S. A., Sanford, T. H., Sheng, X., Turkbey, E. B., Roth, H., Xu, Z., Yang, D., Myronenko, A., Anderson, V., Amalou, A., Blain, M., Kassin, M., Long, D., Varble, N., Walker, S. M., Bagci, U., Lerardi, A. M., Stellato, E., Plensich, G. G., ... Turkbey, B. (2020). Artificial intelligence for the detection of COVID-19 pneumonia on chest CT using multinational datasets. *Nature Communications*, *11*, 4080.

- Hawass, Z., & Saleem, S. N. (2016). *Scanning the pharaohs: CT imaging of the New Kingdom Royal Mummies*. The American University in Cairo Press.
- Hedrick, B. P., Heberling, J. M., Meineke, E. K., Turner, K. G., Grassa, C. J., Park, D. S., Kennedy, J., Clarke, J. A., Cook, J. A., Blackburn, D. C., Edwards, S. V., & Davis, C. C. (2020). Digitization and the future of natural history collections. *Bioscience*, 70, 243–251.
- Hedrick, B. P., Yohe, L., Vander Linden, A., Davalos, L., Sears, K., Sadier, A., Rossiter, S. J., Davies, K. T. J., & Dumont, E. (2018). Assessing soft-tissue shrinkage estimates in museum specimens imaged with diffusible iodine-based contrast-enhanced computed tomography (diceCT). *Microscopy and Microanalysis*, 24, 284–291.
- Herdina, A. N., Herzig-Straschil, B., Hilgers, H., Metscher, B. D., & Plenk, H. (2010). Histomorphology of the penis bone (baculum) in the gray long-eared bat *Plecotus austriacus* (Chiroptera, Vespertilionidae). *The Anatomical Record*, 293, 1248–1258.
- Hesamian, M. H., Jia, W., He, X., & Kennedy, P. (2019). Deep learning techniques for medical image segmentation: Achievements and challenges. *Journal of Digital Imaging*, 32, 582–596.
- Ho, B. H. K., Chen, C. J., Tan, G. J. S., Yeong, W. Y., Tan, H. K. J., Lim, A. Y. H., Ferenczi, M. A., & Mogali, S. R. (2019). Multi-material three dimensional printed models for simulation of bronchoscopy. *BMC Medical Education*, 19, 236.
- Holliday, C. M., Sellers, W. I., Lessner, E. J., Middleton, K. M., Cranor, C., Verhulst, C. D., Lautenschlager, S., Bader, K., Brown, M. A., & Colbert, M. W. (2022). New frontiers in imaging, anatomy, and mechanics of crocodylian jaw muscles. *The Anatomical Record*, 305, 3016–3030.
- Holliday, C. M., Tsai, H. P., Skiljan, R. J., George, I. D., & Pathan, S. (2013). A 3D interactive model and atlas of the jaw musculature of *Alligator mississippiensis*. *PLoS One*, 8, e62806.
- Hoon-Hanks, L. L., Stöhr, A. C., Anderson, A. J., Evans, D. E., Nevarez, J. G., Diaz, R. E., Rodgers, C. P., Cross, S. T., Steiner, H. R., Parker, R. R., & Stenglein, M. D. (2020). Serpentinovirus (Nidovirus) and orthoreovirus coinfection in captive veiled chameleons (*Chamaeleo calytratus*) with respiratory disease. *Viruses*, 12, 1329.
- Hugo, G. D., & Rosu, M. (2012). Advances in 4D radiation therapy for managing respiration: Part I—4D imaging. *Zeitschrift für Medizinische Physik*, 22, 258–271.
- Ivancic, M., Solano, M., & Smith, T. D. (2014). Computed tomography and cross-sectional anatomy of the thorax of the live bottlenose dolphin (*Tursiops truncatus*). *The Anatomical Record*, 297, 901–915.
- Janiesch, C., Zschech, P., & Heinrich, K. (2021). Machine learning and deep learning. *Electronic Markets*, 31, 685–695.
- Juhnke, B., Mattson, A. R., Saltzman, D., Azakie, A., Hoggard, E., Ambrose, M., Iaizzo, P. A., Erdman, A., & Fischer, G. (2019). Use of virtual reality for pre-surgical planning in separation of conjoined twins: A case report. *Journal of Engineering in Medicine*, 233, 1327–1332.
- Kabir, A., Datta, P., Oh, J., Williams, A., Ozbolat, V., Unutmaz, D., & Ozbolat, I. T. (2021). 3D bioprinting for fabrication of tissue models of COVID-19 infection. *Essays in Biochemistry*, 65, 503–518.
- Kassin, M. T., Varble, N., Blain, M., Xu, S., Turkbey, E. B., Harmon, S., Yang, D., Xu, Z., Roth, H., Xu, D., Flores, M., Amalou, A., Sun, K., Kadri, S., Patella, F., Cariati, M., Scarabelli, A., Stellato, E., Lerardi, A. M., ... Wood, B. J. (2021). Generalized chest CT and lab curves throughout the course of COVID-19. *Scientific Reports*, 11, 6940.
- Lawson, A. B., Hedrick, B. P., Echols, S., & Schachner, E. R. (2021). Anatomy, variation, and asymmetry of the bronchial tree in the African grey parrot (*Psittacus erithacus*). *Journal of Anatomy*, 282, 701–719.
- Lee, C. S., Tying, A. J., Deruyter, N. P., Wu, Y., Rokem, A., & Lee, A. Y. (2017). Deep-learning based, automated segmentation of macular edema in optical coherence tomography. *Bio-medical Optics Express*, 8, 3440–3448.
- Li, M., Lei, P., Zeng, B., Li, Z., Yu, P., Fan, B., Wang, C., Li, Z., Zhou, J., Hu, S., & Liu, H. (2020). Coronavirus disease (COVID-19): Spectrum of CT findings and temporal progression of the disease. *Academic Radiology*, 27(5), 603–608.
- Li, X., Cai, H., Cui, X., Cao, P., Zhang, J., Li, G., Li, G., & Zhang, J. (2014). Prevention of late postpneumonectomy complications using a 3D printed lung in dog models. *European Journal of Cardio-Thoracic Surgery*, 46, e67–e73.
- Liu, X., Li, K. W., Yang, R., & Geng, L. S. (2021). Review of deep learning based automatic segmentation for lung cancer radiotherapy. *Frontiers in Oncology*, 11, 717039.
- Liu, X., Song, L., Liu, S., & Zhang, Y. (2021). A review of deep-learning-based medical image segmentation methods. *Sustainability*, 13, 1224.
- Maina, J. N. (2017). Pivotal debates and controversies on the structure and function of the avian respiratory system: Setting the record straight. *Biological Reviews*, 92, 1475–1504.
- Maina, J. N., Singh, P., & Moss, E. A. (2009). Inspiratory aerodynamic valving occurs in the ostrich, *Struthio camelus* lung: A computational fluid dynamics study under resting unsteady state inhalation. *Respiratory Physiology & Neurobiology*, 169, 262–270.
- Maina, J. N., & Woodward, J. D. (2009). Three-dimensional serial section computer reconstruction of the arrangement of the structural components of the parabronchus of the ostrich, *Struthio camelus* lung. *The Anatomical Record*, 292, 1685–1698.
- Makovetsky, R., Piche, N., & Marsh, M. (2018). Dragonfly as a platform for easy image-based deep learning applications. *Microscopy and Microanalysis*, 24, 532–533.
- Malka, S., Hawkins, M. G., Jones, J. H., Pascoe, P. J., Kass, P. H., & Wisner, E. R. (2009). Effect of body position on respiratory system volumes in anesthetized red-tailed hawks (*Buteo jamaicensis*) as measured via computed tomography. *American Journal of Veterinary Research*, 70, 1155–1160.
- Metscher, B. D. (2009a). MicroCT for comparative morphology: Simple staining methods allow high-contrast 3D imaging of diverse non-mineralized animal tissues. *BMC Physiology*, 9, 11.
- Metscher, B. D. (2009b). MicroCT for developmental biology: A versatile tool for high-contrast 3D imaging at histological resolutions. *Developmental Dynamics*, 238, 632–640.
- Meyer, M., Scheid, P., & Piiper, J. (1981). Comparison birds/mammals: Structure and function of the gas exchange apparatus. In: Hutás I, Debreczeni A, editors. Respiration: Proceedings of the

- 28th International Congress of Physiological Sciences, Budapest, 1980. (Advances in physiological sciences). Oxford, England: Pergamon Press. 135–143.
- Molnar, J. L., Diaz, R. E. J., Skorka, T., Dagliyan, G., & Diogo, R. (2017). Comparative musculoskeletal anatomy of chameleon limbs, with implications for the evolution of arboreal locomotion in lizards and for teratology. *Journal of Morphology*, *278*, 1241–1261.
- Moore, M. J., Hammar, T., Arruda, J., Cramer, S., Dennison, S., Montie, E., & Fahlman, A. (2011). Hyperbaric computed tomographic measurement of lung compression in seals and dolphins. *The Journal of Experimental Biology*, *214*, 2390–2397.
- Morrison, R. J., Hollister, S. J., Niedner, M. F., Mahani, M. G., Park, A. H., Mehta, D. K., Ohye, R. G., & Green, G. E. (2015). Mitigation of tracheobronchomalacia with 3D-printed personalized medical devices in pediatric patients. *Science Translational Medicine*, *7*, 285ra264.
- Nevitt, B. N., Langan, J. N., Adkesson, M. J., Mitchell, M. A., HENZLER, M., & Drees, R. (2014). Comparison of air sac volume, lung volume, and lung densities determined by use of computed tomography in conscious and anesthetized Humboldt penguins (*Spheniscus humboldti*) positioned in ventral, dorsal, and right lateral recumbency. *American Journal of Veterinary Research*, *75*, 739–745.
- O'Connor, P. M. O. (2004). Pulmonary pneumaticity in the postcranial skeleton of extant Aves: A case study examining Anseriformes. *Journal of Morphology*, *261*, 141–161.
- Oizumi, H., Kanauchi, N., Kato, H., Endoh, M., Suzuki, J., Fukaya, K., & Sadahiro, M. (2011). Anatomic thoracoscopic pulmonary segmentectomy under 3-dimensional multidetector computed tomography simulation: A report of 52 consecutive cases. *The Journal of Thoracic and Cardiovascular Surgery*, *141*, 678–682.
- Park, B., Park, A. H., Lee, S. M., Seo, J. B., & Kim, N. (2019). Lung segmentation on HRCT and volumetric CT for diffuse interstitial lung disease using deep convolutional neural networks. *Journal of Digital Imaging*, *32*, 1019–1026.
- Park, J., Yun, J., Kim, N., Park, B., Cho, Y., Park, H. J., Song, M., Lee, M., & Seo, J. B. (2020). Fully automated lung lobe segmentation in volumetric chest CT with 3D U-net: Validation with intra- and extra-datasets. *Journal of Digital Imaging*, *33*, 221–230.
- Pattle, R. E., Schock, C., & Creasey, J. M. (1974). Post-mortem changes at electron microscope level in the type II cells of the lung. *British Journal of Experimental Pathology*, *55*, 221–227.
- Ponganis, P. J., St Leger, J., & Scadeng, M. (2015). Penguin lungs and air sacs: Implications for baroprotection, oxygen stores and buoyancy. *The Journal of Experimental Biology*, *218*, 720–730.
- Powell, F. L. (2015). Respiration. In C. G. Scanes (Ed.), *Sturkie's Avian physiology* (pp. 301–336). Elsevier.
- Riquet, M., Mordant, P., Pricopi, C., Legras, A., Foucault, C., Dujon, A., Arame, A., & Le Pimpec-Barthes, F. (2013). A review of 250 ten-year survivors after pneumonectomy for non-small-cell lung cancer. *European Journal of Cardio-Thoracic Surgery*, *45*, 876–881.
- Rosset, A., Spadola, L., & Ratib, O. (2004). OsiriX: An open-source software for navigating in multidimensional DICOM images. *Journal of Digital Imaging*, *17*, 205–216.
- Rubin, G. D., Ryerson, C. J., Haramati, L. B., Sverzellati, N., Kanne, J. P., Raouf, S., Schluger, N. W., Volpi, A., Yim, J. J., Martin, I. B. K., Anderson, D. J., Kong, C., Altes, T., Bush, A., Desai, S. R., Goldin, J., Goo, J. M., Humbert, M., Inoue, Y., ... Leung, A. N. (2020). The role of chest imaging in patient management during the COVID-19 pandemic: A multinational consensus statement from the Fleischner society. *Chest*, *158*, 106–116.
- Saji, H., Inoue, T., Kato, Y., Shimada, Y., Hagiwara, M., Kudo, Y., Akata, S., & Ikeda, N. (2013). Virtual segmentectomy based on high-quality three-dimensional lung modelling from computed tomography images. *Interactive Cardiovascular and Thoracic Surgery*, *17*, 227–232.
- Sanders, R. K., & Farmer, C. G. (2012). The pulmonary anatomy of *Alligator mississippiensis* and its similarity to the avian respiratory system. *The Anatomical Record*, *295*, 699–714.
- Scadeng, M., McKenzie, C., He, W., Bartsch, H., Dubowitz, D. J., Stec, D., & Leger, J. S. (2020). Morphology of the Amazonian teleost genus *Arapaima* using advanced 3D imaging. *Frontiers in Physiology*, *11*, 260.
- Schachner, E. R., Cieri, R. L., Butler, J. P., & Farmer, C. G. (2014). Unidirectional pulmonary airflow patterns in the savannah monitor lizard. *Nature*, *506*, 367–370.
- Schachner, E. R., Diaz, R. E., Coke, R., Echols, S., Osborn, M. L., & Hedrick, B. P. (2022). Architecture of the bronchial tree in Cuvier's dwarf caiman (*Paleosuchus palpebrosus*). *The Anatomical Record*, *305*, 3037–3054.
- Schachner, E. R., Hedrick, B. P., Richbourg, H. R., Hutchinson, J. R., & Farmer, C. G. (2021). Anatomy, ontogeny, and evolution of the archosaurian respiratory system: A case study on *Alligator mississippiensis* and *Struthio camelus*. *Journal of Anatomy*, *238*, 845–873.
- Schachner, E. R., Hutchinson, J. R., & Farmer, C. G. (2013). Pulmonary anatomy in the Nile crocodile and the evolution of unidirectional airflow in Archosauria. *Paleontology and Evolutionary Science*, *1*, e60.
- Schachner, E. R., Sedlmayr, J. C., Schott, R., Lyson, T. R., Sanders, R. K., & Lambertz, M. (2017). Pulmonary anatomy and a case of unilateral aplasia in a common snapping turtle (*Chelydra serpentina*): Developmental perspectives on cryptodiran lungs. *Journal of Anatomy*, *231*, 835–848.
- Schachner, E. R., & Spieler, B. (2020). Three-dimensional (3D) lung segmentation for diagnosis of COVID-19 and the communication of disease impact to the public. *BMJ Case Reports*, *13*, e236943.
- Schumacher, J. (2003). Reptile respiratory medicine. *Veterinary Clinics of North America: Exotic Animal Practice*, *6*, 213–231.
- Shan, Q., Huang, W., Shang, M., Wang, Z., Xia, N., Xue, Q., Wu, Z., Ding, X., Mao, A., & Wang, Z. (2021). Customization of stent design for treating malignant airway stenosis with the aid of three-dimensional printing. *Quantitative Imaging in Medicine and Surgery*, *11*, 1437–1446.
- Simpson, S., Kay, F. U., Abbara, S., Bhalla, S., Chung, J. H., Chung, M., Henry, T. S., Kanne, J. P., Kligerman, S., Ko, J. P., & Litt, H. (2020). Radiological Society of North America expert consensus statement on reporting chest CT findings related to COVID-19. Endorsed by the Society of Thoracic Radiology, the American College of Radiology, and

- RSNA – Secondary Publication. *Journal of Thoracic Imaging*, 2, e200152.
- Smelt, J. L. C., Suri, T., Valencia, O., Jahangiri, M., Rhode, K., Nair, A., & Bille, A. (2019). Operative planning in thoracic surgery: A pilot study comparing imaging techniques and three-dimensional printing. *The Annals of Thoracic Surgery*, 107, 401–406.
- Smith, T. D., Craven, B. A., Engel, S. M., Bonar, C. J., & DeLeon, V. B. (2019). Nasal airflow in the pigmy slow Loris (*Nycticebus pygmaeus*) based on a combined histological, computed tomographic and computational fluid dynamics methodology. *Journal of Experimental Biology*, 222, jeb207605.
- Starmans, M. P. A., van der Voort, S. R., Castillo Tovar, J. M., Veenland, J. F., Klein, S., & Niessen, W. J. (2020). Radiomics: Data mining using quantitative medical image features. In S. K. Zhou, D. Rueckert, & G. Fichtinger (Eds.), *Handbook of medical image computing and computer assisted intervention* (pp. 429–456). Academic Press.
- Sverdlova, N. S., Arkali, F., Witzel, U., & Perry, S. F. (2013). Computational fluid dynamics model of avian tracheal temperature control as a model for extant and extinct animals. *Respiratory Physiology & Neurobiology*, 189, 67–75.
- Tahara, R., & Larsson, H. C. E. (2013). Quantitative analysis of microscopic x-ray computed tomography imaging: Japanese quail embryonic soft tissues with iodine staining. *Journal of Anatomy*, 223, 297–310.
- Tam, M. D., Laycock, S. D., Jayne, D., Babar, J., & Noble, B. (2013). 3-D printouts of the tracheobronchial tree generated from CT images as an aid to management in a case of tracheobronchial chondromalacia caused by relapsing polychondritis. *Journal of Radiology Case Reports*, 7, 34–43.
- Tawhai, M. H., Hunter, P., Tschirren, J., Reinhardt, J., McLennan, G., & Hoffman, E. A. (2004). CT-based geometry analysis and finite element models of the human and ovine bronchial tree. *Journal of Applied Physiology*, 97, 2310–2321.
- Torres-Tamayo, N., García-Martínez, D., Zloliniski, S. L., Torres-Sánchez, I., García-Río, F., & Bastir, M. (2018). 3D analysis of sexual dimorphism in size, shape and breathing kinematics of human lungs. *Journal of Anatomy*, 232, 227–237.
- Ujiie, H., Yamaguchi, A., Gregor, A., Chan, H., Kato, T., Hida, Y., Kaga, K., Wakasa, S., Eitel, C., Clapp, T. R., & Yasufuku, K. (2021). Developing a virtual reality simulation system for pre-operative planning of thoracoscopic thoracic surgery. *Journal of Thoracic Disease*, 13, 778–783.
- Urakubo, H., Bullmann, T., Kubota, Y., Oba, S., & Ishii, S. (2019). UNI-EM: An environment for deep neural network-based automated segmentation of neuronal electron microscopic images. *Scientific Reports*, 9, 19413.
- Vergalasova, I., & Cai, J. (2020). A modern review of the uncertainties in volumetric imaging of respiratory-induced target motion in lung radiotherapy. *Medical Physics*, 47, e988–e1008.
- Waller, J. V., Kaur, P., Tucker, A., Lin, K. K., Diaz, M. J., Henry, T. S., & Hope, M. (2020). Diagnostic tools for coronavirus disease (COVID-19): Comparing CT and RT-PCR viral nucleic acid testing. *American Journal of Roentgenology*, 215, 834–838.
- Wallis, J. W., & Miller, T. R. (1991). Three-dimensional display in nuclear medicine and radiology. *The Journal of Nuclear Medicine*, 32, 534–546.
- Wang, G., Li, W., Zuluaga, M. A., Pratt, R., Patel, P. A., Aertsen, M., Doel, T., David, A. L., Deprest, J., Ourselin, S., & Vercauteren, T. (2018). Interactive medical image segmentation using deep learning with image-specific fine tuning. *IEEE Transactions on Medical Imaging*, 37, 1562–1573.
- Watkins-Colwell, G. J., Love, K., Randall, Z., Boyer, D. M., Winchester, J. M., Stanley, E. L., & Blackburn, D. C. (2018). The walking dead: Status report, data workflow and best practices of the oVert thematic collections network. *Biodiversity Information Science and Standards*, 2, e26078.
- Webster, M. S. (2017). *The extended specimen emerging frontiers in collections-based ornithological research*. CRC Press.
- Wei, J., Xu, H., Xiong, J., Shen, Q., Fan, B., Ye, C., Dong, W., & Hu, F. (2020). 2019 novel coronavirus (COVID-19) pneumonia: Serial computed tomography findings. *Korean Journal of Radiology*, 21, 501–504.
- Werner, R., Ehrhardt, J., Schmidt, R., & Handels, H. (2009). Patient-specific finite element modeling of respiratory lung motion using 4D CT image data. *Medical Physics*, 36, 1500–1511.
- Williams, C. J. A., Hansen, K., Williams, N., Jakobsen, S. R., Pedersen, C. C. E., Bertelsen, M. F., & Wang, T. (2021). The influence of assisted ventilation and recumbency on cardiorespiratory physiology in the anesthetized freshwater turtle *Trachemys scripta scripta*. *Comparative Biochemistry and Physiology, Part A*, 260, 111036.
- Witmer, L. M., Ridgely, R. C., Dufeu, D., & Semones, M. C. (2008). Using CT to peer into the past: 3D visualization of the brain and ear regions of birds, crocodiles, and nonavian dinosaurs. In H. Endo & R. Frey (Eds.), *Anatomical imaging*. Springer.
- Woodward, J. D., & Maina, J. N. (2005). A 3D digital reconstruction of the components of the gas exchange tissue of the lung of the muscovy duck, *Cairina moschata*. *Journal of Anatomy*, 206, 477–492.
- Woodward, J. D., & Maina, J. N. (2008). Study of the structure of the air and blood capillaries of the gas exchange tissue of the avian lung by serial section three-dimensional reconstruction. *Journal of Microscopy*, 230, 84–93.
- Woodward, J. D., Ramonisi, Y., Mashiteng, R., Mokae, L., & Maina, J. N. (2021). Three-dimensional computer reconstruction of the airway- and the vascular systems of the lung of the domestic fowl, *Gallus gallus* variant *domesticus*. *Journal of Applied Mathematics and Computing*, 5, 89–104.
- Xu, C., Sun, G., & Liang, R. (2021). A survey of volume visualization techniques for feature enhancement. *Visual Informatics*, 5, 70–81.
- Ye, Z., Zhang, Y., Wang, Y., Huang, Z., & Song, B. (2020). Chest CT manifestations of new coronavirus disease 2019 (COVID-19): A pictorial review. *European Radiology*, 30, 4381–4389.
- Yoon, S. H., Park, S., Kang, C. H., Park, I. K., Goo, J. M., & Kim, Y. T. (2019). Personalized 3D-printed model for informed consent for stage I lung cancer: A randomized pilot trial. *Seminars in Thoracic and Cardiovascular Surgery*, 31, 316–318.

- York, J. M., Scadeng, M., McCracken, K. G., & Milsom, W. K. (2018). Respiratory mechanics and morphology of Tibetan and Andean high-altitude geese with divergent life histories. *Journal of Experimental Biology*, *221*, 170738.
- Zanaty, E. A., & Ghoniemy, S. (2016). Medical image segmentation techniques: An overview. *International Journal of Informatics and Medical Data Processing*, *1*, 16–37.
- Zhao, W., Zhong, Z., Xie, X., Yu, Q., & Liu, J. (2020). Relation between chest CT findings and clinical conditions of coronavirus disease (COVID-19) pneumonia: A multicenter study. *American Journal of Roentgenology*, *214*, 1072–1077.
- Zhou, S., Wang, Y., Zhu, T., & Xia, L. (2020). CT features of coronavirus disease 2019 (COVID-19) pneumonia in 62 patients in Wuhan, China. *American Journal of Roentgenology*, *214*, 1287–1294.

How to cite this article: Schachner, E. R., Lawson, A. B., Martinez, A., Grand Pre, C. A., Sabottke, C., Abou-Issa, F., Echols, S., Diaz, R. E. Jr, Moore, A. J., Grenier, J.-P., Hedrick, B. P., & Spieler, B. (2023). Perspectives on lung visualization: Three-dimensional anatomical modeling of computed and micro-computed tomographic data in comparative evolutionary morphology and medicine with applications for COVID-19. *The Anatomical Record*, 1–26. <https://doi.org/10.1002/ar.25300>